# Hierarchical porous Fe/Ni-based bifunctional oxygen electrocatalysts for rechargeable zinc-air batteries

Beatrice Ricciardi [a], Williane da Silva Freitas [a], Barbara Mecheri [a,*], Khair Un Nisa [a], Jorge Montero [a], Valerio C.A. Ficca [b], Ernesto Placidi [b], Cinthia Alegre [c], Alessandra D'Epifanio [a]

[a] *Department of Chemical Sciences and Technologies, University of Rome Tor Vergata, Via della Ricerca Scientifica, 00133, Rome, Italy*
[b] *Department of Physics, Sapienza University of Rome, Piazzale Aldo Moro 2, 00185, Rome, Italy*
[c] *Instituto de Carboquímica, CSIC, Calle Miguel Luesma Castán 4, 50018, Zaragoza, Spain*

## ARTICLE INFO

## ABSTRACT

Developing sustainable and efficient bifunctional catalysts for oxygen reduction (ORR) and evolution (OER) reactions is challenging for energy conversion and storage. This work proposes a hierarchical carbon matrix decorated with nitrogen atoms (NC) as a support for obtaining high-performance electrocatalysts based on iron and nickel (Fe/Ni@N–C). The effect of different Fe:Ni ratios and the pyrolysis conditions on the catalyst performance were investigated by combining electrochemical tests, $N_2$-adsorption-desorption, X-ray diffraction, Transmission Electron Microscopy, and X-ray photoelectron spectroscopy. Once optimized the pyrolysis conditions and the Fe:Ni ratio, the Fe/Ni@N–C catalyst showed high bifunctional OER/ORR activity in a three-electrode cell in an alkaline environment (KOH 1 M), with an overall $\Delta E$ for the ORR-OER reaction of 0.75 V. Fe/Ni@N–C was assembled in a rechargeable zinc-air battery, resulting in an excellent electrochemical performance in terms of power density (148.5 $mWcm^{-2}$) and durability, outperforming the benchmark Pt/C–$RuO_2$.

## 1. Introduction

Over the last decades, energy demand has constantly increased, and finding efficient technological approaches to replace fossil fuels is crucial. Moving towards a more sustainable energetic scenario requires developing new technologies capable of efficiently exploiting renewable sources with as low environmental impact as possible [1,2]. $H_2$-fed polymer electrolyte fuel cells and metal-air batteries (MAB) are potential power generation candidates for electric vehicles and flexible devices due to their high energy conversion efficiency, sustainability, and wide availability of raw materials [3–6].

MAB has been recognized as a valid alternative to conventional energy batteries [7,8]. The electrolyte in MAB can be a non-aqueous or aqueous medium, depending on the properties of the metals used at the electrodes. Although batteries with a non-aqueous electrolyte (e.g., lithium-air batteries) are currently more efficient, they often use flammable organic electrolytes, causing safety and environmental issues [9]. In contrast, aqueous electrolytes-based batteries are more sustainable but may be limited by self-corrosion problems in an alkaline environment (e.g., Aluminum-Air (AlAB), Magnesium-Air (MgAB) batteries)

[10,11]. Among MAB, Zinc-Air Batteries (ZAB) are the most advanced nowadays due to their considerable theoretical specific energy, low costs, abundant reserves, and relatively good cycle stability [12–20].

The critical aspect of designing a high-performing ZAB is lowering the reaction barrier for the oxygen reduction reaction (ORR) at the cathode during discharge and improving the oxygen evolution reaction (OER) during recharging [21,22]. The great challenge is, therefore, to develop high-performing bifunctional catalysts that facilitate the slow kinetics of oxygen-related reactions, being stable and cost-effective at the same time. Platinum group metal (PGM)-based materials, particularly Pt/C and $RuO_2$ at alkaline pH, are the reference ORR/OER catalysts due to their high electrochemical activity and efficiency [14,23]. However, their large-scale use is severely limited due to their scarce availability, high cost, and low durability [24,25]. In recent years, enormous efforts have been made to develop ORR, OER, and bifunctional ORR/OER catalysts based on transition metals and nitrogen-doped carbon (M-N-C) [26–36]. Several strategies have been used to enhance catalytic activity, such as the introduction of heteroatoms [37–39], transition single metal site (SMS) [40,41], porous structures [42,43], defects engineering [44,45], and bimetallic doping

approach. This latter strategy is currently most attractive due to the increased flexibility of active sites and the further enhancement of multi-activities [46]. The performance of the catalysts obtained with the bimetallic doping approach depends on the selection of the metal elements and the synthesis methods. Among the various combinations studied in the literature (e.g., Fe-Co [47,48], Zn-Co [49,50], Fe-Mo [51], Fe-Cu [52], and Mn–Fe [53]), the Fe–Ni combination supported on nitrogen-doped carbon matrices shows high catalytic activity for both ORR and OER [54,55]. Despite the advantages of bimetallic doping, the effect of the second metal on the catalysts' electronic structure and the resulting catalytic activity is still ambiguous [40,56].

In our work, Fe/Ni-doped electrocatalysts were prepared using the bimetallic approach on a hierarchically porous carbon matrix decorated with nitrogen (NC). The NC matrix was prepared using a phenolic-melamine resin, resulting in an effective tuning of the N–C functionalities, which is crucial to enhance the introduction of the metal centers, therefore boosting the final catalyst performance toward both ORR and OER.

## 2. Materials and methods

### 2.1. Materials

Melamine (98.0 %), phenol (99.5 %), formaldehyde solution (37 wt % in $H_2O$), iron (II) acetate (95.0 %), nickel (II) acetate (99.9 %), zinc acetate (99 %), $RuO_2$ (99.9 %), Pt/C (40 wt% Pt), sodium hydroxide, potassium hydroxide, Nafion solution (5 wt% in lower aliphatic alcohols and water, 15–20 wt%), polytetrafluoroethylene (PTFE, 60 wt% dispersion in $H_2O$) and 2-propanol were purchased from Sigma-Aldrich. Carbon Vulcan XC-72R was supplied by CABOT Corporation, and carbon paper 38-BC, used as a commercial gas diffusion layer, was purchased from SGL Technologies. Stainless steel woven wire mesh (0.125 mm pore size), used as a current collector, and zinc foil used as an anode was purchased from Goodfellow. Millipore water (18.2 MΩ cm @ 25 °C) was used for the materials preparation and experiments.

### 2.2. Synthesis of the nitrogen-carbon (NC) matrix

0.6 g of phenol and 1.2 g melamine were dissolved in 15 mL of a 0.1 M NaOH solution in DI water and kept under stirring at 50 °C for 30 min. After that, 4.2 mL of formaldehyde was added, and the temperature was raised and kept at 70 °C for 30 min, followed by the addition of 15 mL of a 64 $mgmL^{-1}$ aqueous solution of Pluronic F127 at 60 °C. After 2 h, the reaction mixture was diluted with 50 mL of DI water and kept under stirring at 60 °C overnight. After cooling at room temperature, 30 mL of the resulting solution was diluted with 112 mL of DI water, transferred in a Teflon autoclave, and heated to 120 °C for 24 h. The obtained polymer (NC) was washed by vacuum filtration and dried in a room chamber at 50 °C.

### 2.3. Synthesis of Fe/Ni-based electrocatalysts

300 mg of NC precursor were dispersed in 30 mL of ethanol containing 5 mg of Fe(II) acetate and 19 mg of Ni(II) acetate and kept at room temperature under stirring overnight. The resulting impregnated polymer was dried in an oven at 50 °C and subjected to carbonization through pyrolysis in an inert atmosphere (Ar) at 5 °C $min^{-1}$ up to 250 °C, then 1 °C $min^{-1}$ to 600 °C, hence 10 °C $min^{-1}$ to 900 °C.

After these steps, further heat treatment under different conditions was carried out to obtain five different samples: 20 min $NH_3$ followed by 1 h Ar at 900 °C (2Ni1Fe-NC), 1 h in Ar followed by 20 min $NH_3$ at 900 °C (2Ni1Fe-NC_a), 20 min in $NH_3$ (2Ni1Fe-NC_b), 1 h in Ar (2Ni1Fe-NC_c), and 10 min in Ar (2Ni1Fe-NC_d).

The metal content was determined by inductively coupled plasma (ICP), resulting in 2.5 ± 0.4 wt% of total Fe and Ni content, with a 2:1 Ni:Fe weight ratio. While maintaining the same metal content, the Ni:Fe

weight ratio was reduced to 1:1, adapting the abovementioned procedure and obtaining the 1Ni1Fe-NC sample.

A metal-free sample was also prepared as a control by adopting the same procedure except for the impregnation step of the NC matrix with metal salts (NC_d). Table 1 lists the sample prepared, highlighting the Ni:Fe ratio and pyrolysis conditions.

### 2.4. Preparation of air cathodes

The Fe/Ni-based electrocatalysts were incorporated into air cathodes for ZAB tests. Stainless steel (SS) meshes were used as a current collector, which was modified with a homemade gas diffusion layer (GDL) as follows: 300 mg of Carbon Vulcan were dispersed in 4 mL of ethanol containing 400 μL of PTFE emulsion (40 wt% dispersion in $H_2O$). The obtained thick slurry was homogenously spread on SS mesh (7 $cm^2$) and dried in an oven at 40 °C for 5 min. The GDL-modified SS mesh was hot pressed twice (80 °C and 4.96 MPa) for 1 min. Then, the 38-BC carbon paper (CP), used as commercial GDL, was integrated into the GDL-modified SS mesh and hot pressed under 80 °C and 4.96 MPa for 1 min. The catalyst layer was prepared by dispersing 24 mg of catalyst into a Nafion 5 wt% (160 μL) and isopropanol solution (200 μL), and the ink was deposited onto CP by brush painting to a catalyst loading of 3.14 $mgcm^{-2}$. The prepared cathodes were air-dried overnight and hot pressed (80 °C and 4.96 MPa) for 2 min. According to the same procedure, an air-cathode based on Pt/C–$RuO_2$ with (Pt:$RuO_2$ 1:1 wt ratio) was prepared with a 1 $mgcm^{-2}$ of catalyst loading and used as a control.

### 2.5. Methods of investigation

Thermogravimetric analysis (TGA) was performed by using a thermogravimetric analyzer TGA/DSC1 Star System (Mettler Toledo) working between 25 and 1000 °C under an $N_2$ flow, with a heating rate of 20 °C $min^{-1}$. The materials were held in a platinum sample holder with a cover having one central vent hole.

$N_2$-adsorption-desorption analysis was performed by Micromeritics® TriStar II Plus, Brunauer-Emmett-Teller (BET) method was used to calculate the specific surface area, and the pore volume was deduced by the adsorbed quantity of nitrogen at $P/P_0 = 0.99$. The pore size distribution was calculated by the Barrett-Joyner-Halenda (BJH) model of the desorption isotherm. Samples were carefully prepared before measurements to remove possible impurities that might have been adsorbed in the air; they were kept at 250 °C for 4 h under vacuum and then placed in sample holders to measure $N_2$ desorption.

Transmission electron microscope (TEM) images were acquired with a Tecnai F30 microscope operated at 300 kV, alongside images obtained in the Scanning-Transmission mode with a High Angle Annular Dark Field detector (STEM-HAADF). The samples were ultrasonically dispersed in ethanol for 15 min and then placed in a Cu carbon grid.

Scanning Electron Micrographs (SEM) were obtained using a Leo Supra 35 field-emission scanning electron microscope (Carl Zeiss, Oberkochen, Germany).

Powder X-ray diffraction (XRD) patterns were recorded using a Philips PW1730 diffractometer with Cu Kα radiation (λ = 1.5406 Å).

The surface chemical composition was evaluated through X-ray Photoelectron Spectroscopy (XPS) analysis using a SPECS PHOIBOS 150

**Table 1**
Samples' label, including metal ratio and pyrolysis conditions.

| Samples | Metal ratio (Ni:Fe) | Pyrolysis condition |
|---|---|---|
| **1Ni1Fe-NC** | 1:1 | 20 min. $NH_3$, 1 h Ar |
| **2Ni1Fe-NC** | 2:1 | 20 min. $NH_3$, 1 h Ar |
| **2Ni1Fe-NC_a** | 2:1 | 1 h Ar, 20 min. $NH_3$ |
| **2Ni1Fe-NC_b** | 2:1 | 20 min. $NH_3$ |
| **2Ni1Fe-NC_c** | 2:1 | 1 h Ar |
| **2Ni1Fe-NC_d** | 2:1 | 10 min. Ar |
| **NC_d** | / | 10 min. Ar |

XPS system and monochromatic Al K$_\alpha$ (14866 eV) X-ray source with a 2D CMOS true counting detector. The system was calibrated using Au4f spectra at 84 eV. The powder samples were placed in a custom-made sample holder of electrolytic Cu sputtered with Au. For each sample, the measurements involved a full survey and five different Core levels, namely C1s, O1s, N1s, Fe2p, and Ni2p. The fittings were performed using Kalibri KolXPD software to get a set of constrained parameters for each element to be used in every sample. Asymmetric components were fitted using a Doniach-Sunjic peak, while Ni2p was evaluated using a set of fits for each chemical state, as reported in the XPS methodology found in the Supporting Information.

Electrochemical tests were performed using a standard three-electrode cell: either a rotating ring disk electrode (RRDE-AFE6R2GCPT, Pine Research Instrumentation) or a rotating disk electrode (RDE-AFE4R2GCPT Pine Research Instrumentation) was used as working electrode (WE), whereas a graphite rod as counter electrode (CE) and saturated silver/silver chloride electrode (Ag/AgCl 3.3 M) as a reference electrode (RE). The measurements were recorded with a VMP3 Potentiostat (Bio Logic Science Instruments) controlled by a computer through EC-Lab V10.18 software. The potential values for all electrochemical tests were measured vs. Ag/AgCl (3.3 M) and converted to the reversible hydrogen electrode (RHE).

Before the electrochemical test, the WE was polished with an alumina slurry (0.05 μm particle size). The catalysts inks were prepared by dispersing 3.4 mg of catalyst in 425 mL of a 2-propanol and 75 μL Nafion/H$_2$O solution (0.5 wt%). The suspension was ultrasonicated for 2 h at room temperature. The ink was then drop-casted onto the glassy carbon disk of the WE to a catalyst loading of 0.20 mgcm$^{-2}$ and dried in a ventilated oven at 40 °C for 1 min.

RuO$_2$ and Pt/C (40 wt% Pt) were used as benchmark catalysts for OER and ORR, respectively. RuO$_2$ ink was prepared according to the following formulation: 2 mg RuO$_2$ (99.9 %), 150 μL 2-propanol, 14 μL DI water and 6 μL Nafion (5 wt%). The total loading was 0.28 mgcm$^{-2}$. The Pt/C ink was prepared following the formulation of 1 mg of Pt/C (40 wt % Pt), 630 μL Milli-Q, 220 μL 2-propanol, 150 μL Nafion (0.5 wt%)/H$_2$O) with a Pt/C loading of 40 μgcm$^{-2}$ (16 μgcm$^{-2}$ Pt). Before deposition on the WE, the ink was treated in an ultrasonic bath at 15 °C for 1 h.

The tests were performed in a three-electrode setup with 1 M KOH as electrolyte solution purged with N$_2$ for 20 min. Before testing, the catalysts were activated by cyclic voltammetry (CV) in a potential window of 1.2–0.3 V *vs.* RHE at a scan rate of 500 mVs$^{-1}$ (200 cycles).

After purging the electrolyte with either nitrogen or oxygen, linear sweep voltammetry (LSV) curves were acquired with RDE and RRDE to evaluate the OER and ORR performance. Experiments were run at a scan rate of 10 mVs$^{-1}$ and a rotation speed of 1600 rpm from 1.0 to 0.0 V vs. RHE in O$_2$-saturated to evaluate ORR and from 1.8 to 1.0 V in N$_2$-saturated condition for OER tests [57].

Disk and ring currents were background corrected by subtracting the capacitive current measured in N$_2$-saturated electrolyte, and the potentials reported were *i*R-compensated. The number of electrons transferred (*n*) and hydroperoxide anion (HO$_2^-$) produced were calculated according to Eqs. (1) and (2), where N is the ring collection efficiency (0.26).

$$n = \frac{4 \times |I_{Disk}|}{|I_{Disk}| + |I_{Ring}/N|} \tag{1}$$

$$HO_2^-(\%) = \frac{200 \times |I_{Ring}/N|}{|I_{Disk}| + |I_{Ring}/N|} \tag{2}$$

ZAB tests were performed by assembling the air cathodes prepared as described in the 2.3 section into an in-house ZAB prototype, realized by sealing four plexiglass (5x5x0.5 cm) sheets with Viton rubber gaskets. 1 mm thick zinc foil served as an anode, and 7 mL of an aqueous solution of 0.2 M Zn(CH$_3$COO)$_2$ in 6.0 M KOH was used as an electrolyte. Polarization and power density curves were obtained using a multichannel

VSP potentiostat/galvanostat (BioLogic, France) connected with a computer operating the EC-Lab software. The tests were carried out using a two-electrode configuration with the cathode connected to the working electrode channel and the anode connected to the counter and reference electrode channel. The cycling stability and efficiency were evaluated by the galvanostatic charge-discharge mode at a current density of 5 mAcm$^{-2}$ for 20 min per cycle. The round-trip efficiency (η) was calculated by dividing the voltage recorded during the discharge process by the voltage recorded during the charging process.

The polarization curves were recorded through a linear sweep voltammetry test using a scan rate of 100 mVs$^{-1}$. The power density and current density generated by ZABs were normalized according to the active cathode geometric surface area (3.14 cm$^2$).

## 3. Results and discussion

### 3.1. Catalyst characterization

Different Fe/Ni-based electrocatalysts were prepared as described in the experimental section, and Fig. 1 shows a schematic of the synthesis strategy.

The stage of polymerization and self-assembly allows obtaining an aerogel polymer with high nitrogen content by polymerizing phenol and melamine, followed by adding a nonionic surfactant as a soft template (Pluronic F127) which formed micro micelles trapped in the polymer structure. The sol-gel product was subjected to a hydrothermal treatment to form an aerogel, used as N-doped carbonaceous support (NC) for the impregnation through dual metal doping, obtaining Ni/Fe-NC samples before pyrolysis (2Ni1Fe-NC_precursor and 1Ni1Fe-NC_precursor with two different Ni:Fe ratios, as described in the experimental section). The heat treatment (pyrolysis) is critical for developing electrocatalysts with a hierarchically porous structure and anchoring metal atom sites onto the carbon matrix. A thermo-gravimetric (TG) analysis was carried out (Fig. S1) on NC and 2Ni1Fe-NC_precursor to optimize pyrolysis conditions. Fig. S1 shows that metal-free and metal-doped precursors underwent substantial weight loss due to the removal of Pluronic F127 between 300 and 400 °C and subsequent carbonization of the polymer [58,59]. Metal-free NC had lower weight loss (68 %) than 2Ni1Fe-NC_precursor (86 %), indicating that the presence of Ni and Fe enhanced carbon decomposition in agreement with previous works [60, 61]. As previously reported, at 900 °C, the graphitization of carbon occurs [62,63]. Based on that, 900 °C was selected as pyrolysis temperature and controlled temperature ramps were used to preserve morphology and avoid the collapse of pores due to surfactant sublimation. The effect of the pyrolysis atmosphere (inert or reactive), time (10–80 min), and Ni:Fe weight ratio on the electrocatalysts' properties was evaluated, obtaining seven different samples as detailed in Table 1. Fig. 2(a–c) and Fig. S2 show the prepared samples' scanning electron microscope (SEM) images.

The comparison of SEM images of metal-based samples (Fig. 2b and c, S2a-e) with those of metal-free sample (Fig. 2a and Fig. S2f) indicates that metal impregnation and the different thermal treatments do not affect the morphology, and all the samples show a spheroidal shape. Furthermore, the pyrolysis treatment in an inert (Ar) atmosphere allows the spheroidal shape to be retained (Fig. 2b and Fig. S2d), while a reactive atmosphere (NH$_3$) partially eroded the NC-supports, as can be seen from Fig. 2c and Fig. S2a, S2b, and S2c.

N$_2$-adsorption-desorption isotherms for all the samples (Fig. 2d) were classified as type IV, typical of mesoporous solids, according to the IUPAC classification [64]. The specific surface area (SSA), estimated according to the BET method, were 571.2 ± 5.4 m$^2$g$^{-1}$, 603.9 ± 6.2 m$^2$g$^{-1}$, 573.9 ± 4.8 m$^2$g$^{-1}$, 501.8 ± 5.1 m$^2$g$^{-1}$ and 510.4 ± 6.4 m$^2$g$^{-1}$ for 2Ni1Fe-NC, 2Ni1Fe-NC_a, 2Ni1Fe-NC_b, 2Ni1Fe-NC_c and 2Ni1Fe-NC_d, respectively. In particular, the samples obtained by a single pyrolysis step under Ar atmosphere (2Ni1Fe-NC_c and 2Ni1Fe-NC_d) had a lower specific surface area than 2Ni1Fe-NC_b obtained by a single pyrolysis
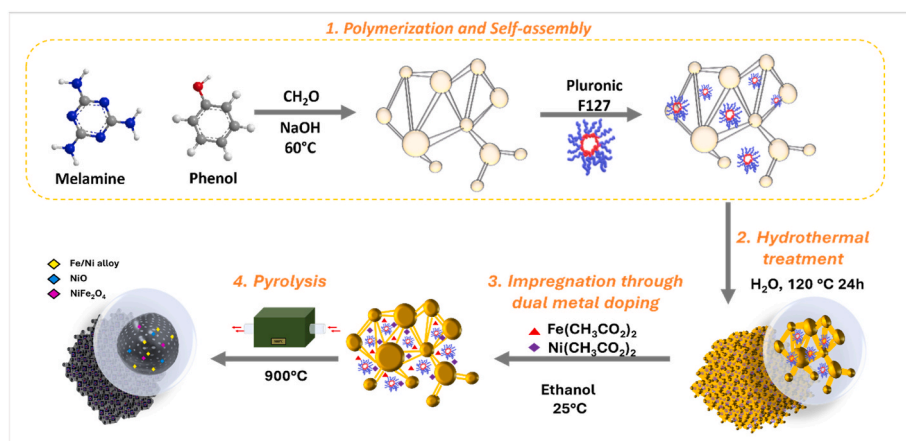
**Fig. 1.** Schematic illustration of the synthesis of Fe/Ni-NC catalysts. (A colour version of this figure can be viewed online.)
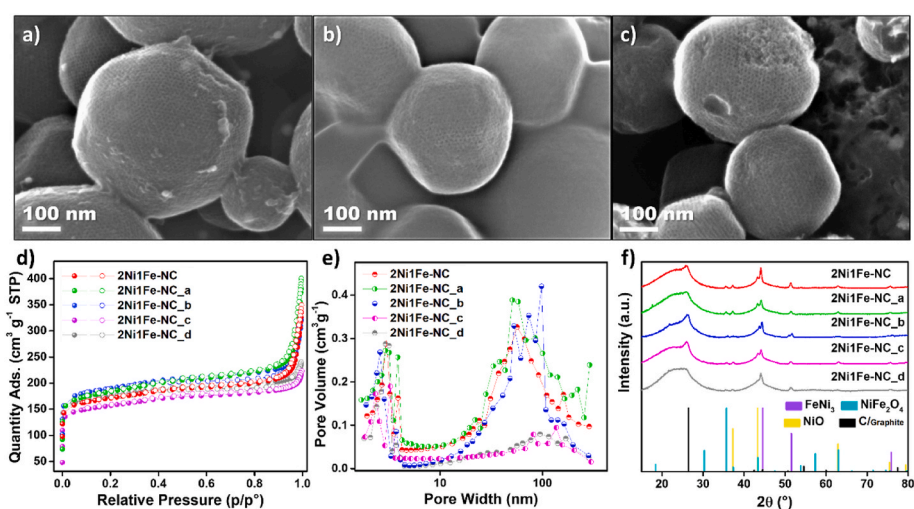


**Fig. 2.** SEM images of NC_d (a), 2Ni1Fe-NC_c (b), and 2Ni1Fe-NC (c). $N_2$-adsorption-desorption isotherms (d), BJH pore-size distribution (e), and XRD patterns of 2Ni1Fe-NC, 2Ni1Fe-NC_a, 2Ni1Fe-NC_b, 2Ni1Fe-NC_c, and 2Ni1Fe-NC_d (f). (A colour version of this figure can be viewed online.)

step under $NH_3$ atmosphere. This trend agrees with previously reported works that confirm the beneficial effect of pyrolysis under the $NH_3$ atmosphere in increasing the porosity and formation of N-based active sites [33,65,66]. When $NH_3$ and Ar were combined into two pyrolysis steps ($NH_3 \rightarrow$ Ar or Ar $\rightarrow NH_3$), the SSA further increased for the sample obtained by a first pyrolysis in Ar followed by a second pyrolysis in $NH_3$ (2Ni1Fe_NC_a); by contrast, if the first pyrolysis is conducted in $NH_3$ followed by a second pyrolysis in Ar (2Ni1Fe_NC), SSA did not significantly increase. This finding can be explained by considering that the first pyrolysis in Ar leads to the development of graphitic shells, which promotes the surface and porosity development in the second pyrolysis step [67–69]. In contrast, when the pyrolysis is first conducted in $NH_3$, the porosity development obtained from the first pyrolysis step is not particularly affected by the second treatment in Ar.

The effect of the pyrolysis atmosphere was also reflected by BJH pore size distribution (Fig. 2e). All samples had a pore size distribution between 1.8 and 4.4 nm in a border zone between micro- (pore width< 2 nm) and meso-pores (2 nm < pore width <50 nm). Moreover, larger pores can also be observed for all samples, except for 2Ni1Fe-NC_c and 2Ni1Fe-NC_d, which exhibited a lower contribution in the BJH range of 39–300 nm.

Fig. 2f and Fig. S3 show XRD patterns, indicating an amorphous carbon component between $2\theta = 21°$–$24°$ and the 002 graphitic plane in the range $2\theta = 24°$–$28°$ (JCPDS Card No. 12–0212) [70] with a different graphitization degree depending on the thermal treatments. Along with enhancing graphitization, the presence of Ni/Fe metals leads to forming metal phases, among which the catalytically active phase of $FeNi_3$ alloy (JCPDS sheet n. 38–0419) is predominant. $NiFe_2O_4$ (JCPDS sheet n. 44–1485) [71,72] and nickel oxide (JCPDS sheet n. 03–1209) [73] phases are also present to a lesser extent.

A first screening of the overall bifunctional electrocatalytic performance of the samples obtained with different pyrolysis treatments was evaluated by the potential difference ($\Delta E_{OER\text{-}ORR}$) between the OER potential values at a current density of 10 mAcm$^{-2}$ ($E_{J10}$) and the ORR half-wave potential values ($E_{1/2}$), obtained from the overall OER-ORR polarization curves shown in Fig. 3. $\Delta E_{OER\text{-}ORR}$ values are listed in Table S1, together with typical $\Delta E$ values previously reported in the literature for other Fe/Ni-based electrocatalysts. The comparison with the literature data highlights that the samples prepared in this work have a good bifunctional OER/ORR activity. In particular, 2Ni1Fe-NC exhibited the lowest $\Delta E$ (0.75 V), outperforming the reported state-of-art bifunctional electrocatalysts and the catalysts obtained in this work with different thermal treatments, pointing to the crucial role of $NH_3$ atmosphere for the formation of catalytically active Fe/Ni–N domains. It is well-known that $NH_3$ gas at high temperatures (>800 °C) with carbon domains produces the N functionalities required to bind iron cations to the carbon support, which is essential in forming active sites [74].
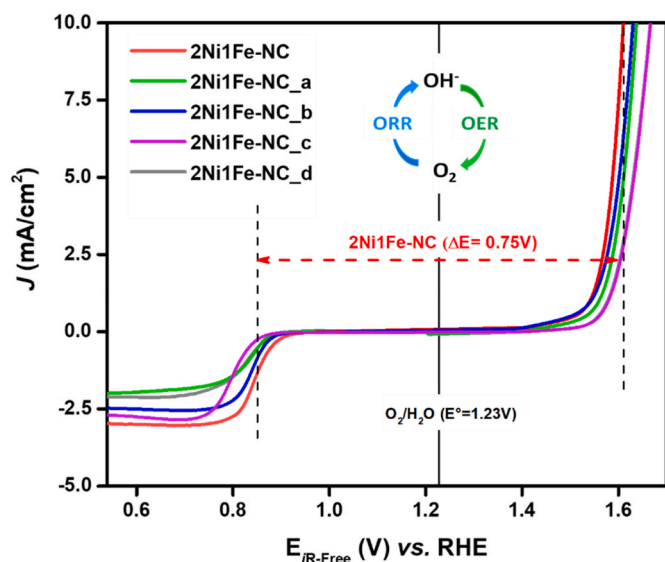
**Fig. 3.** Overall LSV polarization curves of 2Ni1Fe-NC, 2Ni1Fe-NC_a, 2Ni1Fe-NC_b, 2Ni1Fe-NC_c, and 2Ni1Fe-NC_d in 0.1 M KOH at a 10 mVs$^{-1}$ potential scan rate, and 1600 rpm rotation speed. (A colour version of this figure can be viewed online.)

To get deeper insights into the effect of the pyrolysis conditions on the formation of Fe/Ni–N active sites, a sample with an increased Fe:Ni ratio was prepared (1Ni1Fe-NC) with the same thermal treatment as 2Ni1Fe-NC. As pointed out by SEM images and BET analysis (Figs. S4 and S5), 1Ni1Fe-NC had a similar morphological and textural feature as compared to 2Ni1Fe-NC; however, the XRD pattern (Fig. S6) showed structural differences due to the high amount of iron in 1Ni1Fe-NC which increased graphitization and promote the formation of different Ni alloys (Fe$_{0.64}$Ni$_{0.36}$) [75,76]. 2Ni1Fe-NC and 1Ni1Fe-NC samples were further characterized by transmission electron microscopy (TEM) analysis, and the corresponding results are shown in Fig. 4 and Fig. S7, respectively.

Fig. 4a and Fig. S7a show high-angle dark-field scanning electron microscopy (HAADF-STEM) images revealing the presence of homogeneous metal nanoparticles (NPs) on the carbon substrate. The composition of the NPs was further analyzed by energy dispersive X-ray spectroscopy (STEM-EDS) microanalysis (Fig. 4b and Fig. S7b), confirming the formation of Fe/Ni alloys and oxides. TEM analysis (Fig. 4c and Fig. S7c, S8a, and S8b) confirms what has already been observed for the SEM and BET analysis: the porous spherical morphology of the samples was partly preserved despite the reactive NH$_3$ treatment during pyrolysis. Comparing the two samples, the higher Ni content in 2Ni1Fe-NC also catalyzes the formation of carbon nanotubes (CNTs) (Fig. 4d–e). By contrast, this feature is less pronounced in the 1Ni1Fe-NC sample, as seen by comparing Fig. S7e. The shape of CNTs is tubular, undulate hollow with bamboo-like junctions, which is common when there is a strong presence of N on the surface [77–79]. Fig. 4f and Fig. S7f show that the prolonged effect of pyrolysis in Ar induces the formation of carbon shells on some NPs.

The surface chemistry was investigated using XPS upon collection of the surveys, reported in Fig. 5a. High-resolution scans for the identified core levels C1s, N1s, and Ni2p$_{3/2}$, for the most significant samples 1Ni1Fe-NC and 2Ni1Fe-NC, were reported in Fig. 5b–d; instead, deconvolution of O1s and Fe2p spectra were reported in Figs. S9–S10, respectively. All the remaining samples are reported in the Supporting Information, Figs. S11–S15.

The C1s, O1s, and N1s spectra have been fitted using the same criteria employed in previous studies [80–83], but due to the presence of nickel, Ni2p and Fe2p have been managed following the principles present in specific literature for Ni-based compounds [84–86], as thoroughly explained in the Supporting Information (XPS methodology). The chemical speciation of elements for all samples is reported in Tables S2–S6.

The spectra recorded for carbon and nitrogen were peculiar to systems characterized by a high content of graphitic structure (always higher than 50 %) alloyed with N moieties of predominantly pyrrolic form. Indeed, the fit resulted in 93.6 % of C and 3.2 % of N for the 2Ni1Fe-NC_c sample and, respectively 92.4/4.7 %, 92.2/4.1 %, 94.2/3.4 %, and 95.4/1.9 % for the samples 2Ni1Fe-NC_b, 2Ni1Fe-NC_a, 2Ni1Fe-NC and 1Ni1Fe-NC. The oxygen content was usually below 3 %, except for 2Ni1Fe-NC_a (3.4 %). Within the C1s, 2Ni1Fe-NC_a has the lowest C sp$^2$ content (highest disordered C sp$^3$), while 1Ni1Fe-NC has the highest C sp$^2$ content (lowest disordered C sp$^3$). This can be associated with the post-treatment in NH$_3$ of 2Ni1Fe-NC_a, partially disrupting the
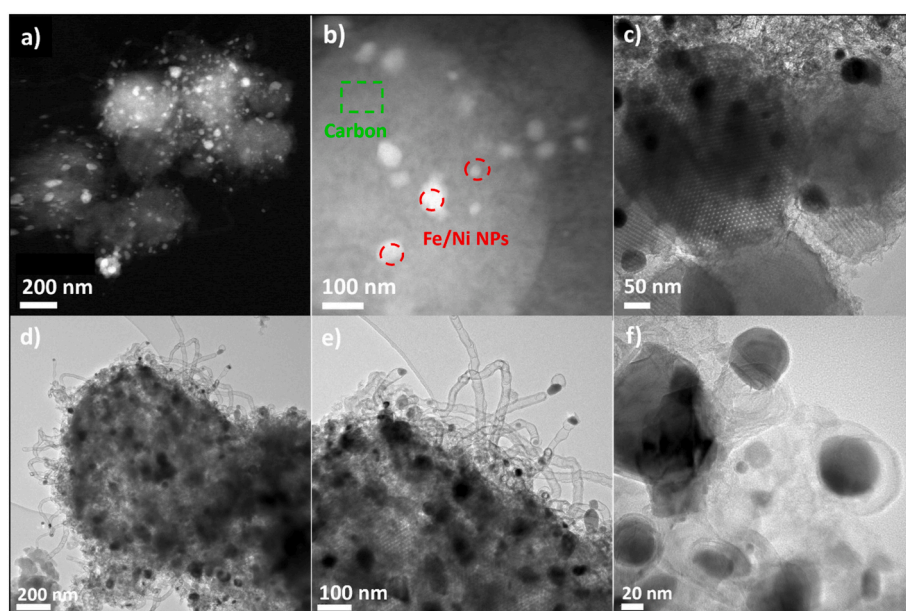


**Fig. 4.** (a) HAADF-STEM, b) STEM-EDS, and (c–f) TEM images at different magnifications of sample 2Ni1Fe-NC. (A colour version of this figure can be viewed online.)
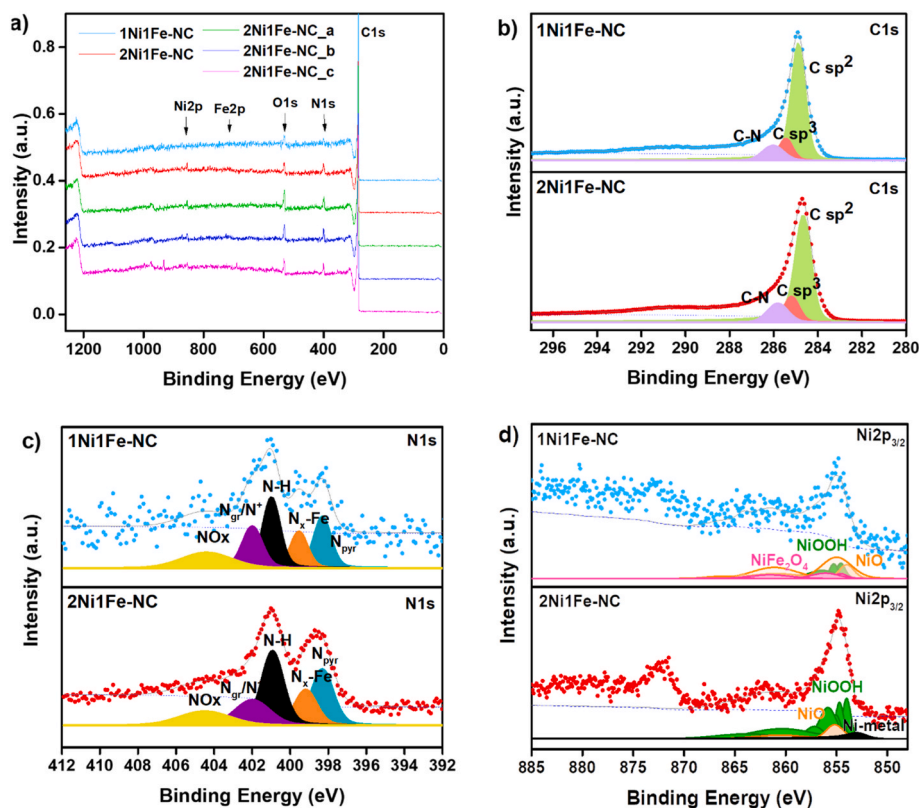
**Fig. 5.** XPS survey scans of the 1Ni1Fe-NC, 2Ni1Fe-NC, 2Ni1Fe-NC_a, 2Ni1Fe-NC_b and 2Ni1Fe-NC_c (a), deconvoluted high-resolution XPS spectra for C 1s (b), N 1s (c) and Ni $2p_{3/2}$ (d) XPS spectra of 1Ni1Fe-NC and 2Ni1Fe-NC. (A colour version of this figure can be viewed online.)

graphitic plane. Other minor components of C1s are C–N, C–O, C=O, and COOH.

The analysis of the N1s XPS spectrum showed that an appreciable component of Fe-$N_x$ or amine can be seen along with pyridinic N. Indeed, the amine moieties overlap at the same BE of Fe-$N_x$, around 399.8 eV [87,88]. Considering the pyrolysis conditions used to prepare our FeNi-based catalysts, the amine presence at the catalysts' surface cannot be excluded, even more so for the samples prepared using $NH_3$ flow as single (2Ni1Fe-NC_b) or last step (2Ni1Fe-NC_a) of pyrolysis, as previously reported by other authors [89–91]. For all samples, the amine/Fe-$N_x$ content is always higher than 2Ni1Fe-NC_c, reaching its maximum with the 2Ni1Fe-NC_a, treated with ammonia after the pyrolysis in argon. In the case of 2Ni1Fe-NC_a, differently than the others, the pyridinic component resulted in a higher amount than pyrrolic N. Regarding 2Ni1Fe-NC and 1Ni1Fe-NC, the post-treatment with Ar reduced the quantity of amine bound to the surface with respect to samples 2Ni1Fe-NC_a and 2Ni1Fe-NC_b.

Regarding Ni2p and the abovementioned assumptions for peaks fitting, the samples were characterized by the presence of a main broad peak located at ~854.8 eV, except for 2Ni1Fe-NC_a, positively shifted of 0.4 eV *ca*, which can be deconvoluted with multiple components. Indeed, according to TEM and XRD results, due to the composition of the systems, containing both Fe and Ni, the fits were thus performed using Ni ferrite ($NiFe_2O_4$), NiOOH, and NiO sets, resulting in percentages of each reported in Table S4. In addition, the surface chemistry investigation of the 2Ni1Fe-NC family provided evidence of minor content of metallic Ni or alloys like $FeNi_3$, possessing the same features of Ni(0), eventually buried under graphitic layers. In the case of sample 1Ni1Fe-NC, Ni ferrite was used instead of metallic Ni because of the differences in composition. The NiOOH phase was not identified in the diffraction patterns, concluding that a higher oxidation state can be found only on the surface. In this case, the maximum content of NiOOH ($Ni^{3+}$) can be found on sample 2Ni1Fe-NC, decreasing in the order 2Ni1Fe-NC >

2Ni1Fe-NC_a > 2Ni1Fe-NC-b > 2Ni1Fe-NC_c, with an opposite trend in NiO content. As a qualitative observation of the peculiar nature of 2Ni1Fe-NC, its satellite structure (about 861 eV) differs from the others, containing shallower components [92,93]. Despite the lower thermal stability of the NiOOH species at high temperatures as compared to oxides and alloy phases, spectroscopical studies demonstrated that their formation and stabilization could be promoted by the presence of nickel oxides at a temperature ranging in between 200 and 650 °C, as previously reported [94–96]. Considering the presence of NiO evidenced even from the XRD analysis, the experimental conditions adopted to prepare the Fe/Ni-based catalysts during the pyrolysis steps, promoted the formation of NiOOH species at the catalyst's surface.

Finally, for Fe2p the signal recorded from all the samples is too low to be accurately fitted to evaluate the chemical speciation of the element. In addition, Auger lines LMM of Ni can be found at 712 eV ($^1$P) and 706 eV ($^3$P), overlapping with the Fe2p spectra. Nevertheless, qualitatively, it is possible to identify a component around 710 eV ascribable to Fe(II) and a second peak associated with iron oxides between 711 and 713 eV [87,97–99].

Overall, the synthesis protocols resulted in highly graphitic samples with N inclusions. This characteristic is common in systems where C-containing compounds are pyrolyzed at high temperatures along with transition metals like Fe, Ni (and Cu). Thus, the low resolution of Fe spectra (but also Ni for 1Ni1Fe-NC) can be associated with the existence of crystalline secondary phases buried under graphitic layers of a few nanometers, creating an external shell grown because of the simultaneous presence of the two metals. Fe-$N_x$ coordination, beneficial for ORR, cannot be excluded, but secondary phases like oxides and Ni alloys impact their formation, modifying the materials and conferring oxygen evolution capabilities. Hence, the ORR performance of the synthesized Ni/Fe-based electrocatalysts can be mainly attributed to a balance between the formation of Fe-$N_x$-C and pyridinic active sites [87,100], combined to the catalytic activity of the iron oxides in highly alkaline

conditions (pH = 14) [101–103]. Although the higher content of Fe-$N_x$/amine moieties has been found for the samples 2Ni1Fe-NC_a and 2Ni1Fe-NC_b (Table S3), their ORR activity was lower than that observed for 2Ni1Fe-NC (Table S1). These results indicate that pyrolysis under $NH_3$ as single (2Ni1Fe-NC_b) or last pyrolysis step (2Ni1Fe-NC_a) led to a higher contribution of inactive amine groups in the lower ORR activity of these catalysts.

Regarding the OER performance, high and comparable OER activity has been reported for both $FeNi_3$ and $Fe_{0.64}Ni_{0.36}$ alloys [104,105], while nickel ferrite ($NiFe_2O_4$) demonstrated to be more active than NiO [106]. The synergistic effect between metallic and oxide-based phases has also been reported to tune the catalyst activity due to strong coupling between FeNi alloys and $NiFe_2O_4$ for electron transfer [107]. Hence, we expect that the OER activity of the prepared Fe/Ni-based samples is dictated by a synergic effect between the metallic alloys and oxides phases combined with oxyhydroxides, together with the possible impact of the in-situ surface reconstruction of metal species during OER [108].

To investigate the bifunctional ORR/OER activity of the Fe/Ni-based samples, polarization curves for 1Ni1Fe-NC and 2Ni1Fe-NC under hydrodynamic conditions were acquired in an alkaline environment (Fig. 6a for ORR and Fig. 6c for OER) and compared with those of the reference Pt/C and $RuO_2$ (Figs. S16 and S17) [23,82]. Fig. 6a shows that the ORR activity for 1Ni1Fe-NC is lower than that observed for 2Ni1Fe-NC, as indicated by the $E_{1/2}$ values (0.83 V and 0.85 V, respectively). This trend was also confirmed when calculating the number of electrons exchanged (*n*) and the peroxide yield ($HO_2^-$) (Fig. S18). For both samples, *n* was around 4 (n = 3.4 for 1Ni1Fe-NC and 3.5 for 2Ni1Fe-NC), and $HO_2^-$ at 0.7 V *vs.* RHE was 31 % and 26 % for 1Ni1Fe-NC and 2Ni1Fe-NC, respectively, indicating that ORR takes place mainly through a $4e^-$ pathway ($O_2 + 4H_2O + 4e^- \rightarrow 4OH^-$). The *n* values lower than 4 can be related to the promotion of an indirect $2 \times 2e^-$ pathway ($O_2 + H_2O + 2e^- \rightarrow OH_2^- + OH^-$; $OH_2^- + H_2O + 2e^- \rightarrow 3OH^-$) [109,110] by the Fe/Ni oxide phases required for the OER activity, that are known to display low activity towards the ORR [111]. The higher

catalytic activity of 2Ni1Fe-NC is in good agreement with the chemical speciation of the N1s XPS spectra, which showed a high content of pyridinic-N and Fe-$N_x$ moieties (highly ORR active) in combination with a low content of nitrogen oxides (poorly ORR active) [112]. The ORR Tafel plots were obtained by plotting *iR*-corrected potential values as a function of the logarithm of the kinetic current density, as shown in Fig. 6b. The plots were linearly fitted from the onset potential values to 0.70 V vs. RHE. The 2Ni1Fe-NC and 1Ni1Fe-NC had a slope of $69 \pm 2$ mVdec$^{-1}$ and $62 \pm 2$ mVdec$^{-1}$, respectively. Based on the ORR mechanism reported in section 3 of the Supporting Information (Page S12), the Tafel slope values are consistent with a rate-determining step (*rds*) due to the formation of $MO_2H$ species [113].

Fig. 6c shows OER polarization curves for 2Ni1Fe-NC and 1Ni1Fe-NC samples. For both samples, the potential value at a current density of 10 mAcm$^{-2}$ ($E_{J10}$) was 1.60 V, indicating that the Ni alloys ($FeNi_3$ and $Fe_{0.64}Ni_{0.36}$) and Ni oxides (NiO and $NiFe_2O_4$), evidenced in both samples by XRD, are active for OER catalysis. However, although the two samples had a similar crystalline phase composition (as evidenced by XRD), they showed a different chemical surface. Based on the literature, the metal species on the surface of the catalysts undergo in situ reconstruction phenomena during OER, and the nickel sites tend to transform into an oxyhydroxide-like active phase responsible for a high OER activity [108,114–116]. Considering the Fe/Ni-based phases of 2Ni1Fe-NC and 1Ni1Fe-NC evidenced by XPS and XRD analysis, the surface reconstruction of $NiFe_2O_4$/NiO (1Ni1Fe-NC) and Ni-metal/NiO (2Ni1Fe-NC) to generate oxyhydroxide species (NiOOH) driven by the anodic potential makes the two catalysts very similar in terms of OER activity.

Although slightly higher than $E_{J10}$ of $RuO_2$ (1.56 V), the overall $\Delta E$ evaluation of bifunctional activity for OER/ORR was very competitive with other PGM-free systems previously reported in the literature (Table S1), especially considering the low content of metals (2.5 % of Fe + Ni) and the synthesis process involving only a polymeric matrix.

The Tafel analysis was carried out to evaluate the *rds* involved in the OER electrocatalysis based on the elementary steps reported in the
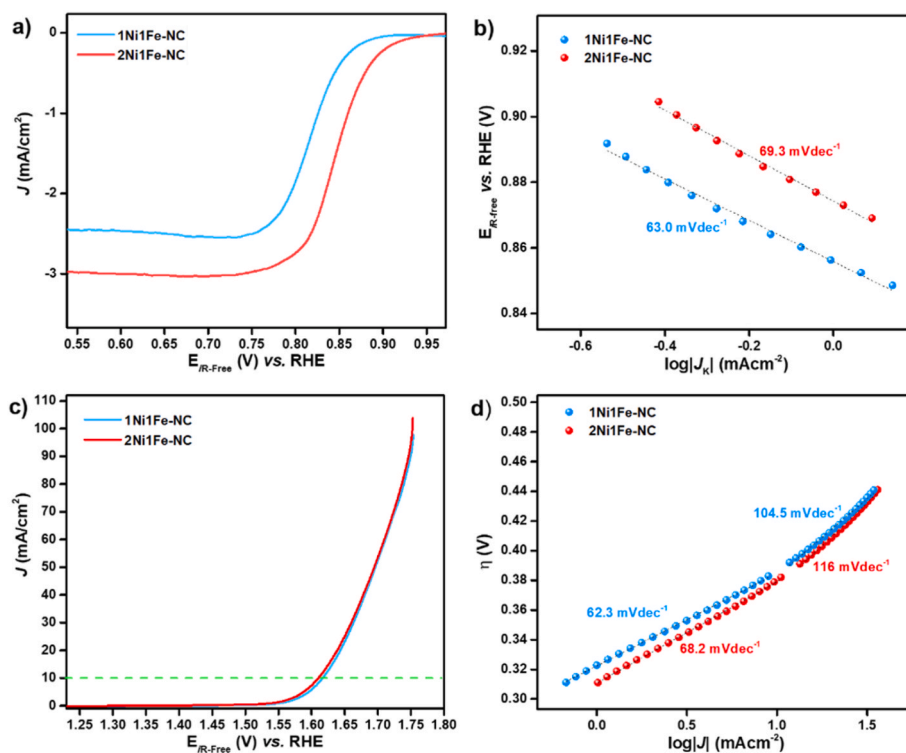


**Fig. 6.** ORR polarization curves in $O_2$-saturated 1 M KOH electrolyte at 1600 rpm and 10 mVs$^{-1}$ (a), ORR Tafel plots (b) OER polarization curves in $N_2$-saturated 1 M KOH electrolyte, at 1600 rpm and 10 mVs$^{-1}$ (c), and OER Tafel plots (d) for 1Ni1Fe-NC and 2Ni1Fe-NC. (A colour version of this figure can be viewed online.)

Supporting Information (Page S12). The Tafel plots (Fig. 6d) were obtained in two linear regions: the onset potential $E_{on}$ and the $E_{J10}$ regions. The slopes in the $E_{on}$ region were between 68.2 and 81.6 mVdec$^{-1}$; according to the theoretical approach of Shinagawa and coworkers [113], those values suggest a possible rate-determining step as MO + OH$^-$ ⇌ MOOH and MOOH + OH$^-$ ⇌ MOO$^-$ + H$_2$O, involving O–O bond formation on the catalyst surface [117]. In the $E_{J10}$ region, the Tafel slopes were between 93.9 and 116 mVdec$^{-1}$ range values, close to the ideal kinetic mechanism according to Antipin et al. [118], a set of concerted surface mechanisms taking place [113,119].

Considering the highly efficient bifunctional catalytic activity of 2Ni1Fe-NC and 1Ni1Fe-NC, a homemade aqueous rechargeable ZAB was assembled, as described in the experimental section. Fig. 7a illustrates two series-connected ZABs equipped with the Fe/Ni cathodes powering several LEDs. A ZAB equipped with commercial Pt/C and RuO$_2$ composite (Pt:RuO$_2$ (1:1) weight ratio) as an air cathode was also assembled for comparison.

Polarization and power density curves, obtained immediately after assembling the ZAB, are depicted in Fig. 7b: the open circuit voltage ($E_{OC}$) for Pt/C–RuO$_2$ based cathode resulted in a higher potential (1.5 V) than both 2Ni1Fe-NC (1.3 V) and 1Ni1Fe-NC (1.38 V). A higher maximum power density (PD$_{max}$) was obtained for 2Ni1Fe-NC (148.5 mWcm$^{-2}$) in comparison to 1Ni1Fe-NC (137.8 mWcm$^{-2}$), while Pt/C–RuO$_2$-based cathode showed 167 mWcm$^{-2}$ as PD$_{max}$. Polarization and power density curves were acquired also after 150 charge-discharge galvanostatic cycles (Fig. S19) and the results indicated that the power density retention capability at the end of cycling was higher for 2Ni1Fe-NC and 1Ni1Fe-NC (78.8 mWcm$^{-2}$ and 60.5 mWcm$^{-2}$, respectively, as PD$_{max}$), than commercial Pt/C–RuO$_2$ (53.7 mWcm$^{-2}$). This finding demonstrates a superior long-term stability of Fe/Ni-based cathodes

than PGM cathodes. Galvanostatic cycling at a current of 5 mAcm$^{-2}$ with 10-min discharging 10-min charging intervals are shown in Fig. 7c and d. The magnified view of the charge-discharge cycles (Fig. 6c) indicates a slight difference in the discharge potential values during the first cycles (1.25 V for 2Ni1Fe-NC and 1.23 V for 1Ni1Fe-NC), due to the higher ORR activity of 2Ni1Fe-NC than 1Ni1Fe-NC (Fig. 5a). Despite this similar performance trend observed in both half-cell tests and ZAB tests, the significant ORR performance difference of 2Ni1Fe-NC and 1Ni1Fe-NC is not strictly reflected in the ZAB polarization curves; in fact, as previously reported in the literature [120–123], along with the catalyst activity, other factors such as the cell configuration, electrolyte and oxygen concentration, and preparation of the catalyst ink, play a key role in influencing the activation, ohmic, and concentration polarizations, and resulting in severe performances discrepancies [124].

Moreover, a similar initial difference in charge and discharge voltage ($E_{gap}$) for ZABs equipped with 1Ni1Fe-NC, 2Ni1Fe-NC, and Pt/C–RuO$_2$-based air cathodes was observed (0.74 V, 0.68 V, and 0.71 V, respectively). However, after continuous cycling for 150 cycles, a significant increase in $E_{gap}$ (1.14 V) can be observed for the PGM cathodes. In contrast, only a slight $E_{gap}$ increase can be observed for the 2Ni1Fe-NC and 1Ni1Fe-NC air cathodes (0.83 V), showing better long-term cyclability as compared to commercial Pt/C–RuO$_2$. 2Ni1Fe-NC and 1Ni1Fe-NC also showed superior round-trip efficiency (59 %) in comparison to the Pt/C–RuO$_2$ (50 %) at the end of 150 cycles (50 h). The ZAB equipped with Pt/C–RuO$_2$-based air cathodes experienced a voltage loss of 430 mV in contrast to 2Ni1Fe-NC and 1Ni1Fe-NC, which exhibit a voltage loss of 150 mV and 120 mV, respectively. Hence, The NiFe-NC materials demonstrated an enhancement of long-term ZAB performance as compared to commercially available cathodes. Table 2 summarizes the electrochemical parameters extrapolated from the ZAB tests
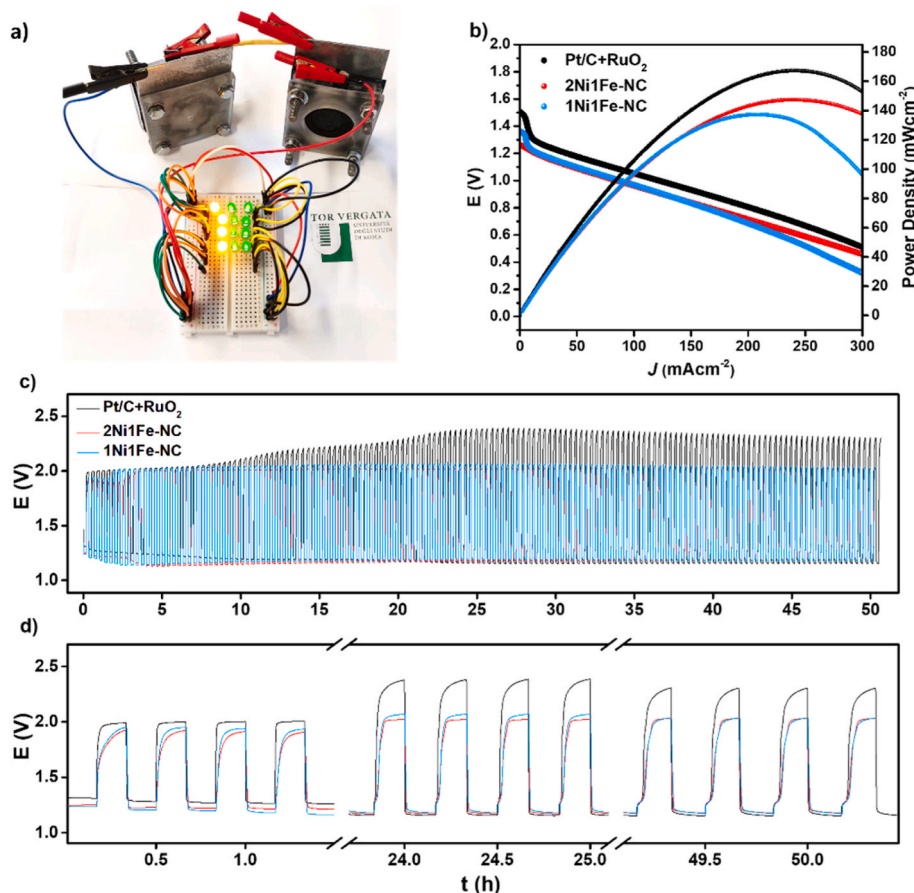


**Fig. 7.** Photograph of light emitting diodes (LEDs) powered by two series-connected ZABs (a), power density and polarization curves (b) galvanostatic charge–discharge cycling profile (150 cycles >50 h) (c) and magnified view charge-discharge cycling profile (d). (A colour version of this figure can be viewed online.)

**Table 2**

Electrochemical parameters extrapolated from ZAB tests: the open circuit voltage ($E_{OC}$), initial maximum power density ($PD_{max}$ (in)), maximum power density after 150 cycles (($PD_{max}$ (cycling)), the difference between charge and discharge voltages during cycles ($E_{gap}$), round-trip efficiency ($\eta$).

| Catalyst | $E_{oc}$ (V) | $PD_{max}$ (in) ($mWcm^{-2}$) | $PD_{max}$ (cycling) ($mWcm^{-2}$) | $E_{gap}$ (V) | $\eta$ (%) |
|---|---|---|---|---|---|
| 2Ni1Fe-NC | 1.30 | $148.5 \pm 2.0$ | $78.8 \pm 1.0$ | 0.83 | 59 |
| 1Ni1Fe-NC | 1.38 | $137.8 \pm 1.0$ | $60.5 \pm 1.5$ | 0.83 | 59 |
| Pt/C + $RuO_2$ | 1.50 | $166.5 \pm 1.7$ | $53.5 \pm 2.0$ | 1.14 | 50 |

for 1Ni1Fe-NC, 2Ni1Fe-NC, and Pt/C–$RuO_2$ based air cathodes.

The performance of Zn-air batteries based on 2Ni1Fe-NC and 1Ni1Fe-NC were compared with other previously reported Zn-air batteries, and the electrochemical parameters are summarized in Table S7. 2Ni1Fe-NC and 1Ni1Fe-NC showed similar or even higher $E_{gap}$ and power density than other metal-nitrogen-carbon-based catalysts previously reported in the literature.

## 4. Conclusions

Hierarchical porous catalysts were produced from a carbon matrix decorated with nitrogen atoms and functionalized with iron and nickel (2.5 wt% total metal content). The Fe/Ni-based electrocatalysts have a spheroidal shape with an extensive and homogeneous porosity, with a different graphitization degree depending on the thermal treatments and the relative Fe/Ni content. The samples had a pore distribution between 1.8 and 4.4 nm in a border zone between micro and mesopores, with a specific surface area in the 500–600 $m^2g^{-1}$.

Tailoring the pyrolysis conditions and the Fe:Ni ratio allowed obtaining a highly graphitic carbon matrix with N inclusions decorated with Fe/Ni functionalities. XRD, XPS and TEM analysis revealed the existence of iron-nitrogen coordination, metal oxide phases and Fe/Ni alloys. As the rotating ring-disk electrode experiments indicated, the materials exhibited oxygen reduction activity, the ORR preceding mainly through a direct (4e$^-$) pathway promoted by Fe-$N_x$ active sites. The existence of FeNi alloys and the corresponding oxides confers oxygen evolution capability to the materials, also considering the reconstruction phenomenon on metal species during OER to generate an oxyhydroxide-like active phase responsible for oxygen evolution activity.

Given the excellent bifunctional oxygen reduction and evolution activity ($\Delta E_{OER-ORR} = 0.75$ V), the electrocatalysts were integrated as air cathodes into a rechargeable zinc-air battery, with promising results. In fact, the materials presented enhanced long-term stability and power density retention than commercial platinum—group-based cathodes after being cycled 150 times for more than 50 h at 5 $mAcm^{-2}$.

## CRediT authorship contribution statement

**Beatrice Ricciardi:** Data curation, Formal analysis, Investigation, Writing – original draft. **Williane da Silva Freitas:** Data curation, Investigation, Methodology, Writing – review & editing. **Barbara Mecheri:** Conceptualization, Investigation, Methodology, Project administration, Resources, Supervision, Writing – review & editing. **Khair Un Nisa:** Data curation, Investigation, Visualization. **Jorge Montero:** Data curation, Investigation, Visualization. **Valerio C.A. Ficca:** Data curation, Investigation, Writing – original draft. **Ernesto Placidi:** Funding acquisition, Investigation, Resources, Writing – review & editing. **Cinthia Alegre:** Investigation, Resources, Writing – review & editing. **Alessandra D'Epifanio:** Conceptualization, Funding acquisition, Investigation, Methodology, Resources, Supervision, Writing – review & editing.

## Declaration of competing interest

The authors declare that they have no known competing financial interests or personal relationships that could have appeared to influence the work reported in this paper.

## Appendix A. Supplementary data

Supplementary data to this article can be found online at https://doi.org/10.1016/j.carbon.2023.118781.

## References

[1] W. Cheng, X. Zhao, H. Su, F. Tang, W. Che, H. Zhang, Q. Liu, Lattice-strained metal–organic-framework arrays for bifunctional oxygen electrocatalysis, Nat. Energy 4 (2019) 115–122, https://doi.org/10.1038/s41560-018-0308-8.

[2] N.S. Lewis, D.G. Nocera, Powering the planet: chemical challenges in solar energy utilization, Proc. Natl. Acad. Sci. U.S.A. 103 (2006) 15729–15735, https://doi.org/10.1073/pnas.0603395103.

[3] K. Jiao, J. Xuan, Q. Du, Z. Bao, B. Xie, B. Wang, Y. Zhao, L. Fan, H. Wang, Z. Hou, S. Huo, N.P. Brandon, Y. Yin, M.D. Guiver, Designing the next generation of proton-exchange membrane fuel cells, Nature 595 (2021) 361–369, https://doi.org/10.1038/s41586-021-03482-7.

[4] D. Banham, T. Kishimoto, Y. Zhou, T. Sato, K. Bai, J.I. Ozaki, Y. Imashiro, S. Ye, Critical advancements in achieving high power and stable nonprecious metal catalyst-based MEAs for real-world proton exchange membrane fuel cell applications, Sci. Adv. 4 (2018) 1–8, https://doi.org/10.1126/sciadv.aar7180.

[5] S. Hosseini, S. Masoudi Soltani, Y.Y. Li, Current status and technical challenges of electrolytes in zinc–air batteries: an in-depth review, Chem. Eng. J. 408 (2021) 127241, https://doi.org/10.1016/j.cej.2020.127241.

[6] C. Zhao, J. Liu, N. Yao, J. Wang, D. Ren, X. Chen, B. Li, Q. Zhang, Can aqueous zinc–air batteries work at sub-zero temperatures? Angew. Chem. 133 (2021) 15409–15413, https://doi.org/10.1002/ange.202104171.

[7] L. Jiang, X. Luo, D.W. Wang, A review on system and materials for aqueous flexible metal–air batteries, Carbon Energy 5 (2023), https://doi.org/10.1002/cey2.284.

[8] E.V. Timofeeva, C.U. Segre, G.S. Pour, M. Vazquez, B.L. Patawah, Aqueous air cathodes and catalysts for metal–air batteries, Curr. Opin. Electrochem. 38 (2023) 101246, https://doi.org/10.1016/j.coelec.2023.101246.

[9] J. Lai, Y. Xing, N. Chen, L. Li, F. Wu, R. Chen, Electrolytes for rechargeable lithium–air batteries, Angew. Chem. Int. Ed. 59 (2020) 2974–2997, https://doi.org/10.1002/anie.201903459.

[10] J. Ren, J. Ma, J. Zhang, C. Fu, B. Sun, Electrochemical performance of pure Al, Al–Sn, Al–Mg and Al–Mg–Sn anodes for Al-air batteries, J. Alloys Compd. 808 (2019) 151708, https://doi.org/10.1016/j.jallcom.2019.151708.

[11] F.W. Richey, B.D. McCloskey, A.C. Luntz, Mg anode corrosion in aqueous electrolytes and implications for Mg-air batteries, J. Electrochem. Soc. 163 (2016) A958–A963, https://doi.org/10.1149/2.0781606jes.

[12] Y. Li, J. Lu, Metal-air batteries: will they Be the future electrochemical energy storage device of choice? ACS Energy Lett. 2 (2017) 1370–1377, https://doi.org/10.1021/acsenergylett.7b00119.

[13] H.F. Wang, C. Tang, Q. Zhang, A review of precious-metal-free bifunctional oxygen electrocatalysts: rational design and applications in Zn−Air batteries, Adv. Funct. Mater. 28 (2018) 1–22, https://doi.org/10.1002/adfm.201803329.

[14] S. Tharani, D. Durgalakshmi, A.K. Kunhiraman, S. Balakumar, R.A. Rakkesh, Hybrid zinc-air battery (ZAB) with transition metal-based electrocatalysts—a step toward next-generation electrochemical energy storage, WIREs Energy Environ (2023) 1–20, https://doi.org/10.1002/wene.472.

[15] C. Lai, H. Li, Y. Sheng, M. Zhou, W. Wang, M. Gong, K. Wang, K. Jiang, 3D spatial combination of CN vacancy-mediated NiFe-PBA with N-doped carbon nanofibers network toward free-standing bifunctional electrode for Zn–air batteries, Adv. Sci. 9 (2022) 1–10, https://doi.org/10.1002/advs.202105925.

[16] J. Xue, S. Deng, R. Wang, Y. Li, Efficient synergistic effect of trimetallic organic frameworks derived as bifunctional catalysis for the rechargeable zinc-air flow battery, Carbon N. Y. 205 (2023) 422–434, https://doi.org/10.1016/j.carbon.2023.01.034.

[17] R. Wu, X. Wang, L. Ge, Z. Zheng, Y. Zhu, C. Zhou, J. Yuan, S. Zhu, Y. Gu, W. Zhou, Z. Shao, N, S co-doped carbon with embedment of FeNi alloy as bifunctional oxygen electrocatalysts for rechargeable Zinc-air batteries, Carbon N. Y. 202 (2023) 141–149, https://doi.org/10.1016/j.carbon.2022.10.047.

[18] Y. Deng, J. Zheng, B. Liu, Y. Liu, H. Li, M. Yang, Schiff-base polymer derived ultralong FeCo/N-doped carbon nanotubes as bifunctional oxygen electrocatalyst for liquid and flexible all-solid-state rechargeable zinc–air batteries, Carbon N. Y. 210 (2023) 118000, https://doi.org/10.1016/j.carbon.2023.04.006.

[19] J.C. Li, Y. Meng, H. Zhong, L. Zhang, S. Ding, Z. Lyu, S.P. Beckman, P.X. Hou, Y. Mei, H.M. Cheng, C. Liu, Supramolecular complex derived carbon nanotubes decorated with iron single atoms and nanoclusters as efficient bifunctional oxygen electrocatalysts for rechargeable Zn-air batteries, Carbon N. Y. 205 (2023) 302–309, https://doi.org/10.1016/j.carbon.2023.01.024.

[20] K. Wang, C. Qiu, Z. Wang, Q. Chen, J. Pan, J. Li, M. Wu, H. Dong, K. Shi, Q. Liu, Job-synergistic engineering from Fe3N/Fe sites and sharp-edge effect of hollow star-shaped nitrogen-doped carbon structure for high-performance zinc-air batteries, Carbon N. Y 214 (2023) 118333, https://doi.org/10.1016/j.carbon.2023.118333.

[21] H.F. Wang, Q. Xu, Materials design for rechargeable metal-air batteries, Matter 1 (2019) 565–595, https://doi.org/10.1016/j.matt.2019.05.008.

[22] Q. Liu, R. Liu, C. He, C. Xia, W. Guo, Z.L. Xu, B.Y. Xia, Advanced polymer-based electrolytes in zinc–air batteries, eScience 2 (2022) 453–466, https://doi.org/10.1016/J.ESCI.2022.08.004.

[23] T.D. Nguyen, G.G. Scherer, Z.J. Xu, A facile synthesis of size-controllable IrO2 and RuO2 nanoparticles for the oxygen evolution reaction, Electrocatalysis 7 (2016) 420–427, https://doi.org/10.1007/s12678-016-0321-2.

[24] K. Ravindra, L. Bencs, R. Van Grieken, Platinum group elements in the environment and their health risk, Sci. Total Environ. 318 (2004) 1–43, https://doi.org/10.1016/S0048-9697(03)00372-3.

[25] V. Balaram, Rare earth elements: a review of applications, occurrence, exploration, analysis, recycling, and environmental impact, Geosci. Front. 10 (2019) 1285–1303, https://doi.org/10.1016/j.gsf.2018.12.005.

[26] X. Xu, Y. Pan, L. Ge, Y. Chen, X. Mao, D. Guan, M. Li, Y. Zhong, Z. Hu, V. K. Peterson, M. Saunders, C. Te Chen, H. Zhang, R. Ran, A. Du, H. Wang, S. P. Jiang, W. Zhou, Z. Shao, High-performance perovskite composite electrocatalysts enabled by controllable interface engineering, Small 17 (2021) 1–10, https://doi.org/10.1002/smll.202101573.

[27] X. Xu, W. Wang, W. Zhou, Z. Shao, Recent advances in novel nanostructuring methods of perovskite electrocatalysts for energy-related applications, Small Methods 2 (2018) 1–35, https://doi.org/10.1002/smtd.201800071.

[28] Z.C. Yao, T. Tang, J.S. Hu, L.J. Wan, Recent advances on nonprecious-metal-based bifunctional oxygen electrocatalysts for zinc-air batteries, Energy Fuel. 35 (2021) 6380–6401, https://doi.org/10.1021/acs.energyfuels.1c00275.

[29] Y.L. Zhang, K. Goh, L. Zhao, X.L. Sui, X.F. Gong, J.J. Cai, Q.Y. Zhou, H. Da Zhang, L. Li, F.R. Kong, D.M. Gu, Z.B. Wang, Advanced non-noble materials in bifunctional catalysts for ORR and OER toward aqueous metal-air batteries, Nanoscale 12 (2020) 21534–21559, https://doi.org/10.1039/d0nr05511e.

[30] B. Mecheri, V.C.A. Ficca, M.A. Costa de Oliveira, A. D'Epifanio, E. Placidi, F. Arciprete, S. Licoccia, Facile synthesis of graphene-phthalocyanine composites as oxygen reduction electrocatalysts in microbial fuel cells, Appl. Catal. B Environ. 237 (2018) 699–707, https://doi.org/10.1016/j.apcatb.2018.06.031.

[31] F. Shahbazi Farahani, B. Mecheri, M.R. Majidi, E. Placidi, A. D'Epifanio, Carbon-supported Fe/Mn-based perovskite-type oxides boost oxygen reduction in bioelectrochemical systems, Carbon N. Y. 145 (2019) 716–724, https://doi.org/10.1016/j.carbon.2019.01.083.

[32] V.C.A. Ficca, C. Santoro, A. D'Epifanio, S. Licoccia, A. Serov, P. Atanassov, B. Mecheri, Effect of active site poisoning on Iron−Nitrogen−Carbon platinum-group-metal-free oxygen reduction reaction catalysts operating in neutral media: a rotating disk electrode study, Chemelectrochem 7 (2020) 3044–3055, https://doi.org/10.1002/celc.202000754.

[33] W. da S. Freitas, A. D'Epifanio, V.C.A. Ficca, E. Placidi, F. Arciprete, B. Mecheri, Tailoring active sites of iron-nitrogen-carbon catalysts for oxygen reduction in alkaline environment: effect of nitrogen-based organic precursor and pyrolysis atmosphere, Electrochim. Acta 391 (2021) 138899, https://doi.org/10.1016/j.electacta.2021.138899.

[34] C. Alegre, C. Busacca, A. Di Blasi, O. Di Blasi, A.S. Aricò, V. Antonucci, V. Baglio, Toward more efficient and stable bifunctional electrocatalysts for oxygen electrodes using FeCo2O4/carbon nanofiber prepared by electrospinning, Mater. Today Energy 18 (2020), https://doi.org/10.1016/j.mtener.2020.100508.

[35] J.C. Ruiz-Cornejo, D. Sebastián, J.I. Pardo, M.V. Martínez-Huerta, M.J. Lázaro, Sulfur-doped carbon nanofibers as support for tantalum oxides bifunctional catalysts for the oxygen reduction and evolution reactions, J. Power Sources 546 (2022) 231988, https://doi.org/10.1016/j.jpowsour.2022.231988.

[36] C. Alegre, C. Busacca, A. Di Blasi, O. Di Blasi, A.S. Aricò, V. Antonucci, V. Baglio, Electrocatalysis of oxygen on bifunctional nickel-cobaltite spinel, Chemelectrochem 7 (2020) 124–130, https://doi.org/10.1002/celc.201901584.

[37] K. Yuan, D. Lützenkirchen-Hecht, L. Li, L. Shuai, Y. Li, R. Cao, M. Qiu, X. Zhuang, M.K.H. Leung, Y. Chen, U. Scherf, Boosting oxygen reduction of single iron active sites via geometric and electronic engineering: nitrogen and phosphorus dual coordination, J. Am. Chem. Soc. 142 (2020) 2404–2412, https://doi.org/10.1021/jacs.9b11852.

[38] J. Zhang, Y. Zhao, C. Chen, Y.C. Huang, C.L. Dong, C.J. Chen, R.S. Liu, C. Wang, K. Yan, Y. Li, G. Wang, Tuning the coordination environment in single-atom catalysts to achieve highly efficient oxygen reduction reactions, J. Am. Chem. Soc. 141 (2019) 20118–20126, https://doi.org/10.1021/jacs.9b09352.

[39] J. Chen, H. Huang, R. Cao, L. Li, X. Tang, B. Wu, Y. Wu, T. Hu, K. Yuan, Y. Chen, Steering local electronic configuration of Fe–N–C-based coupling catalysts via ligand engineering for efficient oxygen electroreduction, Adv. Funct. Mater. 33 (2023) 1–9, https://doi.org/10.1002/adfm.202209315.

[40] R.Y. Fan, H.Y. Zhao, Z.Y. Zhao, W.H. Hu, X. Liu, J.F. Yu, H. Hu, Y.M. Chai, B. Dong, Effective regulation mechanisms of Fe-Ni(oxy)hydroxide: Ni-rich heteroatomic bonding (Ni—O—Fe—O—Ni) is essential, Nano Res. (2022), https://doi.org/10.1007/s12274-022-5019-6.

[41] H.B. Zhang, Y. Meng, H. Zhong, L. Zhang, S. Ding, L. Fang, T. Li, Y. Mei, P.X. Hou, C. Liu, S.P. Beckman, Y. Lin, H.M. Cheng, J.C. Li, Bulk preparation of free-standing single-iron-atom catalysts directly as the air electrodes for high-performance zinc-air batteries, Carbon Energy 5 (2023) 1–10, https://doi.org/10.1002/cey2.289.

[42] X. Wan, X. Liu, Y. Li, R. Yu, L. Zheng, W. Yan, H. Wang, M. Xu, J. Shui, Fe–N–C electrocatalyst with dense active sites and efficient mass transport for high-performance proton exchange membrane fuel cells, Nat. Catal. 2 (2019) 259–268, https://doi.org/10.1038/s41929-019-0237-3.

[43] X. Tang, Y. Wei, W. Zhai, Y. Wu, T. Hu, K. Yuan, Y. Chen, Carbon nanocage with maximum utilization of atomically dispersed iron as efficient oxygen electroreduction nanoreactor, Adv. Mater. 8 (2022) 1–13, https://doi.org/10.1002/adma.202208942.

[44] Z. Jiang, M. Jing, X. Feng, J. Xiong, C. He, M. Douthwaite, L. Zheng, W. Song, J. Liu, Z. Qu, Stabilizing platinum atoms on CeO2 oxygen vacancies by metal-support interaction induced interface distortion: mechanism and application, Appl. Catal. B Environ. 278 (2020) 119304, https://doi.org/10.1016/j.apcatb.2020.119304.

[45] J. Wan, W. Chen, C. Jia, L. Zheng, J. Dong, X. Zheng, Y. Wang, W. Yan, C. Chen, Q. Peng, D. Wang, Y. Li, Defect effects on TiO2 nanosheets: stabilizing single atomic site Au and promoting catalytic properties, Adv. Mater. 30 (2018) 1–8, https://doi.org/10.1002/adma.201705369.

[46] Q. Shao, P. Wang, X. Huang, Opportunities and challenges of interface engineering in bimetallic nanostructure for enhanced electrocatalysis, Adv. Funct. Mater. 29 (2019) 1–23, https://doi.org/10.1002/adfm.201806419.

[47] J. Wang, Z. Huang, W. Liu, C. Chang, H. Tang, Z. Li, W. Chen, C. Jia, T. Yao, S. Wei, Y. Wu, Y. Li, Design of N-coordinated dual-metal sites: a stable and active Pt-free catalyst for acidic oxygen reduction reaction, J. Am. Chem. Soc. 139 (2017) 17281–17284, https://doi.org/10.1021/jacs.7b10385.

[48] G. Zhang, Y. Jia, C. Zhang, X. Xiong, K. Sun, R. Chen, W. Chen, Y. Kuang, L. Zheng, H. Tang, W. Liu, J. Liu, X. Sun, W.F. Lin, H. Dai, A general route via formamide condensation to prepare atomically dispersed metal-nitrogen-carbon electrocatalysts for energy technologies, Energy Environ. Sci. 12 (2019) 1317–1325, https://doi.org/10.1039/c9ee00162j.

[49] Z. Lu, B. Wang, Y. Hu, W. Liu, Y. Zhao, R. Yang, Z. Li, J. Luo, B. Chi, Z. Jiang, M. Li, S. Mu, S. Liao, J. Zhang, X. Sun, An isolated zinc–cobalt atomic pair for highly active and durable oxygen reduction, Angew. Chem. Int. Ed. 58 (2019) 2622–2626, https://doi.org/10.1002/anie.201810175.

[50] Z. Wang, X. Jin, C. Zhu, Y. Liu, H. Tan, R. Ku, Y. Zhang, L. Zhou, Z. Liu, S. J. Hwang, H.J. Fan, Atomically dispersed Co2-N6 and Co-N4 costructures boost oxygen reduction reaction in both alkaline and acidic media, Adv. Mater. 33 (2021) 2104718, https://doi.org/10.1002/adma.202104718.

[51] L. Lin, Z.K. Yang, Y.F. Jiang, A.W. Xu, Nonprecious bimetallic (Fe,Mo)-N/C catalyst for efficient oxygen reduction reaction, ACS Catal. 6 (2016) 4449–4454, https://doi.org/10.1021/acscatal.6b00535.

[52] Y. Sun, Z. Yang, P. Tian, Y. Sheng, J. Xu, Y.F. Han, Oxidative degradation of nitrobenzene by a Fenton-like reaction with Fe-Cu bimetallic catalysts, Appl. Catal. B Environ. 244 (2019) 1–10, https://doi.org/10.1016/j.apcatb.2018.11.009.

[53] T. Li, H. Wang, Y. Yang, H. Xiang, Y. Li, Effect of manganese on the catalytic performance of an iron-manganese bimetallic catalyst for light olefin synthesis, J. Energy Chem. 22 (2013) 624–632, https://doi.org/10.1016/S2095-4956(13)60082-0.

[54] Y. Cheng, S. He, J.P. Veder, R. De Marco, S. ze Yang, S. Ping Jiang, Atomically dispersed bimetallic FeNi catalysts as highly efficient bifunctional catalysts for reversible oxygen evolution and oxygen reduction reactions, Chemelectrochem 6 (2019) 3478–3487, https://doi.org/10.1002/celc.201900483.

[55] J. Yan, M. Tian, R. Shi, T. Gu, K. Zeng, J. Zhou, Q. Zhang, M.H. Rümmeli, R. Yang, Enhanced dual atomic Fe-Ni sites in N-doped carbon for bifunctional oxygen electrocatalysis, Mater. Today Energy 30 (2022) 101171, https://doi.org/10.1016/j.mtener.2022.101171.

[56] C.C.L. McCrory, S. Jung, J.C. Peters, T.F. Jaramillo, Benchmarking heterogeneous electrocatalysts for the oxygen evolution reaction, J. Am. Chem. Soc. 135 (2013) 16977–16987, https://doi.org/10.1021/ja407115p.

[57] A.C. Garcia, M.T.M. Koper, Effect of saturating the electrolyte with oxygen on the activity for the oxygen evolution reaction, ACS Catal. 8 (2018) 9359–9363, https://doi.org/10.1021/acscatal.8b01447.

[58] J. Yu, M. Guo, F. Muhammad, A. Wang, G. Yu, H. Ma, G. Zhu, Simple fabrication of an ordered nitrogen-doped mesoporous carbon with resorcinol-melamine-formaldehyde resin, Microporous Mesoporous Mater. 190 (2014) 117–127, https://doi.org/10.1016/j.micromeso.2014.02.009.

[59] J. Gong, X. Chen, T. Tang, Recent progress in controlled carbonization of (waste) polymers, Prog. Polym. Sci. 94 (2019) 1–32, https://doi.org/10.1016/j.progpolymsci.2019.04.001.

[60] D. Menga, J.L. Low, Y.S. Li, I. Arčon, B. Koyutürk, F. Wagner, F. Ruiz-Zepeda, M. Gaberšček, B. Paulus, T.P. Fellinger, Resolving the dilemma of Fe-N-C catalysts by the selective synthesis of tetrapyrrolic active sites via an imprinting strategy, J. Am. Chem. Soc. 143 (2021) 18010–18019, https://doi.org/10.1021/jacs.1c04884.

[61] P.G. Santori, F.D. Speck, J. Li, A. Zitolo, Q. Jia, S. Mukerjee, S. Cherevko, F. Jaouen, Effect of pyrolysis atmosphere and electrolyte pH on the oxygen reduction activity, stability and spectroscopic signature of FeN x moieties in Fe-N-C catalysts, J. Electrochem. Soc. 166 (2019) F3311–F3320, https://doi.org/10.1149/2.0371907jes.

[62] M. Xie, J. Yang, J. Liang, X. Guo, W. Ding, In situ hydrothermal deposition as an efficient catalyst supporting method towards low-temperature graphitization of amorphous carbon, Carbon N. Y. 77 (2014) 215–225, https://doi.org/10.1016/j.carbon.2014.05.024.

[63] F. Jaouen, S. Marcotte, J.P. Dodelet, G. Lindbergh, Oxygen reduction catalysts for polymer electrolyte fuel cells from the pyrolysis of iron acetate adsorbed on various carbon supports, J. Phys. Chem. B 107 (2003) 1376–1386, https://doi.org/10.1021/jp021634q.

[64] K.S.W. Sing, Adsorption methods for the characterization of porous materials, Adv. Colloid Interface Sci. 76–77 (1998) 3–11, https://doi.org/10.1016/S0001-8686(98)00038-4.

[65] U.I. Kramm, M. Lefèvre, N. Larouche, D. Schmeisser, J.P. Dodelet, Correlations between mass activity and physicochemical properties of Fe/N/C catalysts for the ORR in PEM fuel cell via 57Fe Mössbauer spectroscopy and other techniques, J. Am. Chem. Soc. 136 (2014) 978–985, https://doi.org/10.1021/ja410076f.

[66] S. Hong Lee, J. Kim, D. Young Chung, J. Mun Yoo, H. Seok Lee, M. Jeong Kim, B. Simon Mun, S. Gu Kwon, Y.-E. Sung, T. Hyeon, Design principle of Fe–N–C electrocatalysts: how to optimize multimodal porous structures? J. Am. Chem. Soc. 141 (2019) 2035–2045, https://doi.org/10.1021/jacs.8b11129.

[67] U.I. Kramm, M. Lefèvre, N. Larouche, D. Schmeisser, J.-P. Dodelet, Correlations between mass activity and physicochemical properties of Fe/N/C catalysts for the ORR in PEM fuel cell via 57Fe mössbauer spectroscopy and other techniques, J. Am. Chem. Soc. 136 (2014) 978–985, https://doi.org/10.1021/ja410076f.

[68] Y. Huang, Y. Chen, M. Xu, T. Asset, P. Tieu, A. Gili, D. Kulkarni, V. De Andrade, F. De Carlo, H.S. Barnard, A. Doran, D.Y. Parkinson, X. Pan, P. Atanassov, I. V. Zenyuk, Catalysts by pyrolysis: direct observation of chemical and morphological transformations leading to transition metal-nitrogen-carbon materials, Mater. Today 47 (2021) 53–68, https://doi.org/10.1016/J.MATTOD.2021.02.006.

[69] X. Zhang, F. Yang, D. Tian, H. Zhao, R. Wang, W.M. Lau, Atomic scale evolution of graphitic shells growth via pyrolysis of cobalt phthalocyanine, Adv. Mater. Interfac. 7 (2020) 1–7, https://doi.org/10.1002/admi.202001112.

[70] K. Li, Q. Liu, H. Cheng, M. Hu, S. Zhang, Classification and carbon structural transformation from anthracite to natural coaly graphite by XRD, Raman spectroscopy, and HRTEM, Spectrochim. Acta Part A Mol. Biomol. Spectrosc. 249 (2021) 119286, https://doi.org/10.1016/j.saa.2020.119286.

[71] G. Hou, J. Wu, T. Li, J. Lin, B. Wang, L. Peng, T. Yan, L. Hao, L. Qiao, X. Wu, Nitrogen-rich biomass derived three-dimensional porous structure captures FeNi metal nanospheres: an effective electrocatalyst for oxygen evolution reaction, Int. J. Hydrogen Energy 47 (2022) 12487–12499, https://doi.org/10.1016/j.ijhydene.2022.02.004.

[72] Y. Tang, Y. Lei, G. Li, T. Fu, Y. Xiang, J. Sha, H. Yang, P. Yu, Y. Si, C. Guo, Positive regulation of active sites for oxygen evolution reactions by encapsulating NiFe2O4 nanoparticles in N-doped carbon nanotubes in situ to construct efficient bifunctional oxygen catalysts for rechargeable Zn-air batteries, J. Mater. Chem. A 10 (2022) 5305–5316, https://doi.org/10.1039/d1ta10881f.

[73] H.A. Miller, Green hydrogen from anion exchange membrane water electrolysis, Curr. Opin. Electrochem. 36 (2022) 101122, https://doi.org/10.1016/j.coelec.2022.101122.

[74] M. Lefèvre, E. Proietti, F. Jaouen, J.P. Dodelet, Iron-Based catalysts with improved oxygen reduction activity in polymer electrolyte fuel cells, Science 324 (2009) 71–74, https://doi.org/10.1126/science.1170051, 80-.

[75] R.D. Hunter, J. Ramírez-Rico, Z. Schnepp, Iron-catalyzed graphitization for the synthesis of nanostructured graphitic carbons, J. Mater. Chem. A 10 (2022) 4489–4516, https://doi.org/10.1039/d1ta09654k.

[76] P.J. Yang, T.H. Li, H. Li, A.L. Dang, L. Yuan, Progress in the graphitization and applications of modified resin carbons, Xinxing Tan Cailiao/New Carbon Mater. 38 (2023) 96–110, https://doi.org/10.1016/S1872-5805(23)60715-2.

[77] G.L. Tian, Q. Zhang, B. Zhang, Y.G. Jin, J.Q. Huang, D.S. Su, F. Wei, Toward full exposure of "active sites": nanocarbon electrocatalyst with surface enriched nitrogen for superior oxygen reduction and evolution reactivity, Adv. Funct. Mater. 24 (2014) 5956–5961, https://doi.org/10.1002/adfm.201401264.

[78] H. Liu, Y. Zhang, R. Li, X. Sun, S. Désilets, H. Abou-Rachid, M. Jaidann, L. S. Lussier, Structural and morphological control of aligned nitrogen-doped carbon nanotubes, Carbon N. Y. 48 (2010) 1498–1507, https://doi.org/10.1016/J.CARBON.2009.12.045.

[79] X. Bao, J. Wang, X. Lian, H. Jin, S. Wang, Y. Wang, Ni/nitrogen-doped graphene nanotubes acted as a valuable tailor for remarkably enhanced hydrogen evolution performance of platinum-based catalysts, J. Mater. Chem. A 5 (2017) 16249–16254, https://doi.org/10.1039/c7ta01240c.

[80] V.C.A. Ficca, C. Santoro, E. Placidi, F. Arciprete, A. Serov, P. Atanassov, B. Mecheri, Exchange current density as an effective descriptor of poisoning of active sites in platinum group metal-free electrocatalysts for oxygen reduction reaction, ACS Catal. 13 (2023) 2162–2175, https://doi.org/10.1021/acscatal.2c05222.

[81] W. da Silva Freitas, B. Mecheri, C. Lo Vecchio, I. Gatto, V. Baglio, V.C.A. Ficca, A. Patra, E. Placidi, A. D'Epifanio, Metal-organic-framework-derived electrocatalysts for alkaline polymer electrolyte fuel cells, J. Power Sources 550 (2022) 232135, https://doi.org/10.1016/J.JPOWSOUR.2022.232135.

[82] B. Ricciardi, B. Mecheri, W. da Silva Freitas, V.C.A. Ficca, E. Placidi, I. Gatto, A. Carbone, A. Capasso, A. D'Epifanio, Porous iron-nitrogen-carbon electrocatalysts for anion exchange membrane fuel cells (AEMFC), Chemelectrochem 202201115 (2023) 1–12, https://doi.org/10.1002/celc.202201115.

[83] W. da Silva Freitas, A. D'Epifanio, C. Lo Vecchio, I. Gatto, V. Baglio, V.C.A. Ficca, E. Placidi, B. Mecheri, Tailoring MOF structure via iron decoration to enhance ORR in alkaline polymer electrolyte membrane fuel cells, Chem. Eng. J. 465 (2023) 142987, https://doi.org/10.1016/j.cej.2023.142987.

[84] M.C. Biesinger, B.P. Payne, L.W.M. Lau, A. Gerson, R.S.C. Smart, X-ray photoelectron spectroscopic chemical state Quantification of mixed nickel metal, oxide and hydroxide systems, Surf. Interface Anal. 41 (2009) 324–332, https://doi.org/10.1002/sia.3026.

[85] A.P. Grosvenor, M.C. Biesinger, R.S.C. Smart, N.S. McIntyre, New interpretations of XPS spectra of nickel metal and oxides, Surf. Sci. 600 (2006) 1771–1779, https://doi.org/10.1016/j.susc.2006.01.041.

[86] M.C. Biesinger, B.P. Payne, A.P. Grosvenor, L.W.M. Lau, A.R. Gerson, R.S. C. Smart, Resolving surface chemical states in XPS analysis of first row transition metals, oxides and hydroxides: Cr, Mn, Fe, Co and Ni, Appl. Surf. Sci. 257 (2011) 2717–2730, https://doi.org/10.1016/J.APSUSC.2010.10.051.

[87] K. Artyushkova, A. Serov, S. Rojas-Carbonell, P. Atanassov, Chemistry of multitudinous active sites for oxygen reduction reaction in transition metal-nitrogen-carbon electrocatalysts, J. Phys. Chem. C 119 (2015) 25917–25928, https://doi.org/10.1021/acs.jpcc.5b07653.

[88] K. Artyushkova, I. Matanovic, B. Halevi, P. Atanassov, Oxygen binding to active sites of Fe–N–C ORR electrocatalysts observed by ambient-pressure XPS, J. Phys. Chem. C 121 (2017) 2836–2843, https://doi.org/10.1021/acs.jpcc.6b11721.

[89] K. Yokoyama, Y. Sato, M. Yamamoto, T. Nishida, T. Itoh, K. Motomiya, Functionalization of primary amine groups to single-walled carbon nanotubes by reacting fluorinated SWCNTs with ammonia gas at a low temperature, Carbon N. Y. 172 (2021) 360–371, https://doi.org/10.1016/J.CARBON.2020.10.038.

[90] K. Artyushkova, S. Rojas-Carbonell, C. Santoro, E. Weiler, A. Serov, R. Awais, R. Rajeev Gokhale, P. Atanassov, Correlations between synthesis and performance of Fe-based PGM-free catalysts in acidic and alkaline media: evolution of surface chemistry and morphology, ACS Appl. Energy Mater. 2 (2019) 5406–5418, https://doi.org/10.1021/acsaem.9b00331.

[91] C. Santoro, S. Rojas-Carbonell, R. Awais, R. Gokhale, M. Kodali, A. Serov, K. Artyushkova, P. Atanassov, Influence of platinum group metal-free catalyst synthesis on microbial fuel cell performance, J. Power Sources 375 (2018) 11–20, https://doi.org/10.1016/j.jpowsour.2017.11.039.

[92] Y. Zheng, G. Zhang, P. Zhang, S. Chu, D. Wu, C. Sun, B. Qian, S. Chen, S. Tao, L. Song, Structural investigation of metallic Ni nanoparticles with N-doped carbon for efficient oxygen evolution reaction, Chem. Eng. J. 429 (2022) 132122, https://doi.org/10.1016/j.cej.2021.132122.

[93] J. Li, B. Wang, Y. Qin, Q. Tao, L. Chen, MOF-derived Ni@NC catalyst: synthesis, characterization, and application in one-pot hydrogenation and reductive amination, Catal. Sci. Technol. 9 (2019) 3726–3734, https://doi.org/10.1039/c9cy00734b.

[94] K. Kawashima, R.A. Márquez-Montes, H. Li, K. Shin, C.L. Cao, K.M. Vo, Y.J. Son, B.R. Wygant, A. Chunangad, D.H. Youn, G. Henkelman, V.H. Ramos-Sánchez, C. S. Mullins, Electrochemical behavior of a Ni3N OER precatalyst in Fe-purified alkaline media: the impact of self-oxidation and Fe incorporation, Mater. Adv 2 (2021) 2299–2309, https://doi.org/10.1039/d1ma00130b.

[95] Q. Wang, X. Huang, Z. Liang Zhao, M. Wang, B. Xiang, J. Li, Z. Feng, H. Xu, M. Gu, Ultrahigh-loading of Ir single atoms on NiO matrix to dramatically enhance oxygen evolution reaction, J. Am. Chem. Soc. 142 (2020) 7425–7433, https://doi.org/10.1021/jacs.9b12642.

[96] A.R. Blume, W. Calvet, A. Ghafari, T. Mayer, A. Knop-Gericke, R. Schlögl, Structural and chemical properties of NiOx thin films: the role of oxygen vacancies in NiOOH formation in a H2O atmosphere, Phys. Chem. Chem. Phys. 25 (2023) 25552–25565, https://doi.org/10.1039/d3cp02047a.

[97] K. Artyushkova, C. Walker, W. Patterson, P. Atanassov, Hierarchically structured non-PGM oxygen reduction electrocatalyst based on microemulsion-templated silica and pyrolyzed iron and cyanamide precursors, Electrocatalysis 5 (2014) 241–247, https://doi.org/10.1007/s12678-014-0185-2.

[98] A. Serov, K. Artyushkova, P. Atanassov, Fe-N-C oxygen reduction fuel cell catalyst derived from carbendazim: synthesis, structure, and reactivity, Adv. Energy Mater. 4 (2014) 1–7, https://doi.org/10.1002/aenm.201301735.

[99] P. Varshney, R.S. Mishra, N. Kumar, Understanding the nature of passivation film formed during corrosion of Fe39Mn20Co20Cr15Si5Al1 high entropy alloy in 3.5 wt% NaCl solution, J. Alloys Compd. 904 (2022) 164100, https://doi.org/10.1016/j.jallcom.2022.164100.

[100] T. Asset, P. Atanassov, Iron-nitrogen-carbon catalysts for proton exchange membrane fuel cells, Joule 4 (2020) 33–44, https://doi.org/10.1016/j.joule.2019.12.002.

[101] J. Li, Q. Jia, S. Mukerjee, M.T. Sougrati, G. Drazic, A. Zitolo, F. Jaouen, The challenge of achieving a high density of Fe-based active sites in a highly graphitic carbon matrix, Catalysts 9 (2019), https://doi.org/10.3390/catal9020144.

[102] M.M. Hossen, K. Artyushkova, P. Atanassov, A. Serov, Synthesis and characterization of high performing Fe-N-C catalyst for oxygen reduction reaction (ORR) in Alkaline Exchange Membrane Fuel Cells, J. Power Sources 375 (2018) 214–221, https://doi.org/10.1016/j.jpowsour.2017.08.036.

[103] I. Roche, E. Chaînet, M. Chatenet, J. Vondrák, Carbon-supported manganese oxide nanoparticles as electrocatalysts for the oxygen reduction reaction (ORR) in alkaline medium: physical characterizations and ORR mechanism, J. Phys. Chem. C 111 (2006) 1434–1443, https://doi.org/10.1021/jp0647986.

[104] X. Zheng, X. Cao, K. Zeng, J. Yan, Z. Sun, M.H. Rümmeli, R. Yang, A self-jet vapor-phase growth of 3D FeNi@NCNT clusters as efficient oxygen electrocatalysts for zinc-air batteries, Small 17 (2021) 1–10, https://doi.org/10.1002/smll.202006183.

[105] X. Xie, H. Peng, K. Sun, X. Lei, R. Zhu, Z. Zhang, G. Ma, Z. Lei, Rational construction of FeNi3/N doped carbon nanotubes for high-performance and reversible oxygen catalysis reaction for rechargeable Zn-air battery, Chem. Eng. J. 452 (2023) 139253, https://doi.org/10.1016/j.cej.2022.139253.

[106] Ö.N. Avcl, L. Sementa, A. Fortunelli, Mechanisms of the oxygen evolution reaction on NiFe2O4and CoFe2O4inverse-spinel oxides, ACS Catal. 12 (2022) 9058–9073, https://doi.org/10.1021/acscatal.2c01534.

[107] Y. Ma, X. Dai, M. Liu, J. Yong, H. Qiao, A. Jin, Z. Li, X. Huang, H. Wang, X. Zhang, Strongly coupled FeNi alloys/NiFe2O4@Carbonitride layers-assembled microboxes for enhanced oxygen evolution reaction, ACS Appl. Mater. Interfaces 8 (2016) 34396–34404, https://doi.org/10.1021/acsami.6b11821.

[108] H. Ding, H. Liu, W. Chu, C. Wu, Y. Xie, Structural transformation of heterogeneous materials for electrocatalytic oxygen evolution reaction, Chem. Rev. 121 (2021) 13174–13212, https://doi.org/10.1021/acs.chemrev.1c00234.

[109] Y. Sun, L. Silvioli, N.R. Sahraie, W. Ju, J. Li, A. Zitolo, S. Li, A. Bagger, L. Arnarson, X. Wang, T. Moeller, D. Bernsmeier, J. Rossmeisl, F. Jaouen, P. Strasser, Activity-selectivity trends in the electrochemical production of hydrogen peroxide over single-site metal-nitrogen-carbon catalysts, J. Am. Chem. Soc. 141 (2019) 12372–12381, https://doi.org/10.1021/jacs.9b05576.

[110] U. Tylus, Q. Jia, K. Strickland, N. Ramaswamy, A. Serov, P. Atanassov, S. Mukerjee, Elucidating oxygen reduction active sites in pyrolyzed metal-nitrogen coordinated non-precious-metal electrocatalyst systems, J. Phys. Chem. C 118 (2014) 8999–9008, https://doi.org/10.1021/jp500781v.

[111] C. Goswami, K.K. Hazarika, P. Bharali, Transition metal oxide nanocatalysts for oxygen reduction reaction, Mater. Sci. Energy Technol. 1 (2018) 117–128, https://doi.org/10.1016/j.mset.2018.06.005.

[112] W. Zhou, L. Ge, Z.G. Chen, F. Liang, H.Y. Xu, J. Motuzas, A. Julbe, Z. Zhu, Amorphous iron oxide decorated 3D heterostructured electrode for highly efficient oxygen reduction, Chem. Mater. 23 (2011) 4193–4198, https://doi.org/10.1021/cm201439d.

[113] T. Shinagawa, A.T. Garcia-Esparza, K. Takanabe, Insight on Tafel slopes from a microkinetic analysis of aqueous electrocatalysis for energy conversion, Sci. Rep. 5 (2015) 1–21, https://doi.org/10.1038/srep13801.

[114] K.L. Nardi, N. Yang, C.F. Dickens, A.L. Strickler, S.F. Bent, Creating highly active atomic layer deposited NiO electrocatalysts for the oxygen evolution reaction, Adv. Energy Mater. 5 (2015) 1–10, https://doi.org/10.1002/aenm.201500412.

[115] Y. Li, H. Guo, J. Zhao, Y. Zhang, L. Zhao, R. Song, Te-doped NiFe2O4 stabilized by amorphous carbon layers derived from one-step topological transitions of NiFe LDHs with significantly enhanced oxygen evolution reaction, Chem. Eng. J. 464 (2023) 142604, https://doi.org/10.1016/J.CEJ.2023.142604.

[116] G. Zhang, J. Zeng, J. Yin, C. Zuo, P. Wen, H. Chen, Y. Qiu, Iron-facilitated surface reconstruction to in-situ generate nickel–iron oxyhydroxide on self-supported FeNi alloy fiber paper for efficient oxygen evolution reaction, Appl. Catal. B Environ. 286 (2021) 119902, https://doi.org/10.1016/J.APCATB.2021.119902.

[117] D. Böhm, M. Beetz, M. Schuster, K. Peters, A.G. Hufnagel, M. Döblinger, B. Böller, T. Bein, D. Fattakhova-Rohlfing, Efficient OER catalyst with low Ir volume density obtained by homogeneous deposition of iridium oxide nanoparticles on macroporous antimony-doped tin oxide support, Adv. Funct. Mater. 30 (2020), https://doi.org/10.1002/adfm.201906670.

[118] D. Antipin, M. Risch, Calculation of the Tafel slope and reaction order of the oxygen evolution reaction between pH 12 and pH 14 for the adsorbate mechanism, Electrochem. Sci. Adv. (2022) 1–13, https://doi.org/10.1002/elsa.202100213.

[119] C. Rosmini, T. Tsoncheva, D. Kovatcheva, N. Velinov, H. Kolev, D. Karashanova, M. Dimitrov, B. Tsyntsarski, D. Sebastián, M.J. Lázaro, Mesoporous Ce–Fe–Ni nanocomposites encapsulated in carbon-nanofibers: synthesis, characterization and catalytic behavior in oxygen evolution reaction, Carbon N. Y. 196 (2022) 186–202, https://doi.org/10.1016/j.carbon.2022.04.036.

[120] M. Zhang, Q. Dai, H. Zheng, M. Chen, L. Dai, Novel MOF-derived Co@N-C bifunctional catalysts for highly efficient Zn–air batteries and water splitting, Adv. Mater. 30 (2018) 1–10, https://doi.org/10.1002/adma.201705431.

[121] L.L. Tian, J. Yang, M.Y. Weng, R. Tan, J.X. Zheng, H.B. Chen, Q.C. Zhuang, L. M. Dai, F. Pan, Fast diffusion of O2 on nitrogen-doped graphene to enhance oxygen reduction and its application for high-rate Zn-air batteries, ACS Appl. Mater. Interfaces 9 (2017) 7125–7130, https://doi.org/10.1021/acsami.6b15235.

[122] Y. Wang, Y. Yang, S. Jia, X. Wang, K. Lyu, Y. Peng, H. Zheng, X. Wei, H. Ren, L. Xiao, J. Wang, D.A. Muller, H.D. Abruña, B.J. Hwang, J. Lu, L. Zhuang, Synergistic Mn-Co catalyst outperforms Pt on high-rate oxygen reduction for alkaline polymer electrolyte fuel cells, Nat. Commun. 10 (2019) 6–13, https://doi.org/10.1038/s41467-019-09503-4.

[123] K. Muuli, X. Lyu, M. Mooste, M. Käärik, B. Zulevi, J. Leis, H. Yu, D.A. Cullen, A. Serov, K. Tammeveski, Outstanding platinum group metal-free bifunctional catalysts for rechargeable zinc-air batteries, Electrochim. Acta 446 (2023) 142126, https://doi.org/10.1016/J.ELECTACTA.2023.142126.

[124] D. Jiao, Z. Ma, J. Li, Y. Han, J. Mao, T. Ling, S. Qiao, Test factors affecting the performance of zinc–air battery, J. Energy Chem. 44 (2020) 1–7, https://doi.org/10.1016/J.JECHEM.2019.09.008.